

Machine Learning Reveals Lipidome Remodeling Dynamics in a Mouse Model of Ovarian Cancer

Authors

Olatomiwa O. Bifarin^{1,†}, Samyukta Sah^{1,†}, David A. Gaul^{1,4}, Samuel G. Moore⁴, Ruihong Chen², Murugesan Palaniappan^{2,3}, Jaeyeon Kim⁵, Martin M. Matzuk^{2,3}, Facundo M. Fernández^{1,4*}

Affiliations

¹School of Chemistry and Biochemistry, Georgia Institute of Technology, Atlanta, Georgia 30332, United States.

²Department of Pathology & Immunology, Baylor College of Medicine, Houston, TX 77030, United States.

³Center for Drug Discovery, Department of Pathology & Immunology, Baylor College of Medicine, Houston, TX 77030, United States.

⁴Petit Institute of Bioengineering and Bioscience, Georgia Institute of Technology, Atlanta, Georgia 30332, United States.

⁵Department of Biochemistry and Molecular Biology, Indiana University School of Medicine, Indiana University Melvin and Bren Simon Comprehensive Cancer Center, Indianapolis, Indiana, 46202, United States.

*Corresponding author. Email: facundo.fernandez@chemistry.gatech.edu (F.M.F)

† These authors contributed equally to this work.

Abstract

Ovarian cancer (OC) is one of the deadliest cancers affecting the female reproductive system. It may present little or no symptoms at the early stages, and typically unspecific symptoms at later stages. High-grade serous ovarian cancer (HGSC) is the subtype responsible for most ovarian cancer deaths. However, very little is known about the metabolic course of this disease, particularly in its early stages. In this longitudinal study, we examined the temporal course of serum lipidome changes using a robust HGSC mouse model and machine learning data analysis. Early progression of HGSC was marked by increased levels of phosphatidylcholines and phosphatidylethanolamines. In contrast, later stages featured more diverse lipids alterations, including fatty acids and their derivatives, triglycerides, ceramides, hexosylceramides, sphingomyelins, lysophosphatidylcholines, and phosphatidylinositols. These alterations underscored unique perturbations in cell membrane stability, proliferation, and survival during cancer development and progression, offering potential targets for early detection and prognosis of human ovarian cancer.

Teaser

Time-resolved lipidome remodeling in an ovarian cancer model is studied through lipidomics and machine learning.

47 Introduction

48

49 The absence of reliable non-invasive ovarian cancer (OC) diagnostics leads to more deaths
50 than any other cancer associated with the female reproductive system, with 419,085 deaths
51 from 1990 to 2019 in the United States alone (1). It is the fifth leading cause of cancer-
52 related death in women (2). Failure of early detection remains the most daunting challenge
53 in OC diagnosis (3). In the United States, the 5-year survival rate is 93.1% for localized OC,
54 but it is reduced drastically to only 30.8% for metastatic OC (4). High-grade serous ovarian
55 cancer (HGSC) is the most frequent subtype accounting for 70-80% of all OC deaths (5, 6).
56 Early diagnosis is therefore imperative for reducing OC mortality. However, OC often
57 eludes detection until an advanced stage (6) and the molecular pathogenesis underlying
58 early-stage OC remains poorly understood. To study the biochemical underpinnings of
59 early-stage OC pathogenesis, we conducted in-depth lipidomic analyses in a *Dicer1-Pten*
60 double-knockout (DKO) mouse model as a function of time. These mice faithfully
61 recapitulate human HGSC with phenotypic, histopathologic, and molecular similarities (7,
62 8) and exhibit stepwise development and progression of HGSC, beginning with a
63 premalignant phase, tumor initiation, and malignant growth in the primary tissue before
64 advancing to early metastases, widespread metastases, and ultimately death.

65 It is now widely accepted that cancer is a metabolic disease (9). As such,
66 metabolomics/lipidomics are central to cancer biology. Metabolomics and lipidomics allow
67 for measuring and identifying small-molecule metabolites or lipids in complex clinical
68 specimens such as serum and tissue samples (10). Two basic types of metabolomics
69 experiments exist, either targeted or non-targeted (11). These experiments are typically
70 conducted using nuclear magnetic resonance (NMR) spectroscopy and/or mass
71 spectrometry (MS). Non-targeted metabolomics/lipidomics allows for the unbiased
72 detection of thousands of metabolites/lipids, while targeted approaches focus on a known
73 set of target species. For an unbiased discovery investigation of a specific disease, as in this
74 work, non-targeted approaches are typically the first step. Non-targeted workflows lead to
75 the generation of big data, necessitating mining methods such as machine learning. These
76 methods are a subset of artificial intelligence that involve developing systems that can learn
77 and improve with more experience without being explicitly programmed to do so (12).
78 Combining machine learning with metabolomics and lipidomics is a powerful approach to
79 learn about cancer biology (13), providing a unique opportunity for the discovery of
80 candidate prognostic and predictive biomarkers.

81 Multiple studies have attempted to find metabolome or lipidome alterations associated with
82 ovarian cancer in biofluids (14-18). In Gaul *et al.*, using serum metabolomics, serous
83 epithelial ovarian cancer (EOC) was discriminated from healthy controls (HC) (HC $n = 49$,
84 EOC $n = 46$) using 16 metabolites including numerous lipids (14). The discrimination
85 achieved 100% accuracy in the cohort studied using support vector machines (SVM) (14).
86 Braicu and co-workers conducted a serum metabolomics study detailing profound lipid
87 metabolism alterations (15). Serum samples of 147 OC patients were compared with 98
88 control subjects with benign ovarian tumors and non-neoplastic diseases. Improved
89 predictive values were achieved when cancer antigen 125, the current OC clinical
90 biomarker, was used alongside some lipid species identified in the study (15). Metabolomics
91 investigations on ovarian cancer mouse models have also been conducted. Jones *et al.*
92 performed metabolomic serum profiling for the detection of early-stage HGSC in DKO
93 mice, identifying 18 discriminatory metabolites, including lipids in the

94 phosphatidylethanolamine (PE), triglyceride (TG), lysophosphatidylethanolamine
95 (LysoPE), and phosphatidylinositol (PI) classes (19).

96 Here, we present the first in-depth machine learning longitudinal analysis of the serum
97 lipidome of a DKO HGSC mouse model using a four-pronged approach: 1) unsupervised
98 machine learning methods and univariate statistical analyses to map global lipidome
99 alterations, 2) hierarchical clustering analysis to identify lipidome changes in response to
100 HGSC progression, 3) multiple machine learning algorithms with varying inductive biases
101 to identify time-resolved HGSC evolution, and 4) Kaplan-Meier estimates and Restricted
102 Mean Survival Times analyses to find prognostic circulating lipid marker candidates.

103 104 **Results**

105 **Research design and computational pipeline.**

106 To study HGSC development and progression, we employed DKO mice (*Dicer1*^{flox/flox} *Pten*^{flox/flox} *Amhr2*^{cre/+}) and DKO control mice (*Dicer1*^{flox/flox} *Pten*^{flox/flox} *Amhr2*^{+/+}) models
107 using high-density blood sampling (**Figure 1a**). A total of 15 mice in both groups were used
108 for analysis. Starting from the two-month mark, blood samples were collected biweekly
109 until humane sacrifice of the animals, or at the end of the study at 46 weeks. This
110 longitudinal design resulted in 221 and 238 blood samples collected for DKO and DKO
111 control mice, respectively. As expected, DKO mice had a shorter lifespan than DKO control
112 mice, as shown by the Kaplan-Meier (**Figure S1a**) and the Nelson-Aalen (**Figure S1b**)
113 estimate curves. Furthermore, the restricted mean survival time difference (Δ RMST)
114 between DKO and DKO control mice was about three weeks (**Figure S1c**).
115

116 Given the time-course data misalignment, each time point was converted to a “percentage
117 lifetime” variable to align the dataset (**Figure 1b**). The percentage lifetime was computed
118 by taking the percentage of the age of each mouse in weeks normalized by the total lifespan
119 of the mouse (or age of the mice) at the last time point of blood collection (see Methods).
120 Percent lifetimes were binned into five stages, which we named the “lifetime stage”. 0-30%
121 lifetime was named as lifetime stage I (DKO $n = 28$, DKO control $n = 34$), 30-45% lifetime
122 was lifetime stage II (DKO $n = 41$, DKO control $n = 45$), 45-60% lifetime was lifetime stage
123 III (DKO $n = 43$, DKO control $n = 42$), 60-75% lifetime was lifetime stage IV (DKO $n =$
124 41 , DKO control $n = 45$), and 75-100% lifetime was lifetime stage V (DKO $n = 68$, DKO
125 control $n = 72$). Where n refers to the number of time points present in each lifetime stage.

126 The longitudinal lipidomic dataset was then investigated to (1) identify global lipidome
127 alterations between DKO and DKO control mice within these lifetime stages, (2) investigate
128 the longitudinal lipidome evolution in response to HGSC progression, (3) identify lipidome
129 signatures for each of the five lifetime stages *via* supervised ML, and (4) identify prognostic
130 circulating candidate biomarkers *via* survival analysis (**Figure 1c**).

131 **Global lipidomic changes in the DKO HGSC model.**

132 In-depth lipidomic profiling of all 459 serum samples was carried out using reverse-phase
133 (RP) ultra-high performance liquid chromatography-mass spectrometry (UHPLC-MS). A
134 total of 17,293 and 4,414 features (de-adducted and de-isotoped m/z , retention time pairs)
135 were extracted from the RP UHPLC-MS dataset in the positive and negative ion modes,
136 respectively. After data curation and structural annotation, 1070 lipids were identified by
137 matching to an in-house lipid MS² database. The classes of lipids detected included
138 triacylglycerols (TG), fatty acids (FA), hexosylceramides (HexCer),
139

140 lysophosphatidylcholines (LPC), lysophosphatidylethanolamines (LPE),
141 phosphatidylcholines (PC), ether phosphatidylcholines (PC-O), phosphatidylethanolamines
142 (PE), ether phosphatidylethanolamines (PE-O), phosphatidylinositols (PI), ceramides (Cer),
143 sterols, and sphingomyelins (SM). **Figure 2a** shows fold changes (Log_2FC [DKO/control])
144 for all 1070 annotated lipids and time points combined, indicating significant lipidome
145 remodeling. Of the 1070 compounds annotated, 87 lipids (**Table S1**) had corrected P -values
146 lower than 0.05 (Welch's T -test, Benjamini-Hochberg (BH) correction q -value < 0.05).
147 Some of the top-most altered lipids included HexCer(d34:1), PE(O-37:6), PE(O-36:6), and
148 FA(14:1) (**Figure 2b**).

149
150 To investigate global differences between DKO and DKO control mice, the 87 significant
151 lipids were used to conduct unsupervised learning for all combined time points. PCA
152 (**Figure S2a**), kernel PCA (**Figure S2b**), t-SNE (**Figure S2c**), and uMAP (**Figure S2d**)
153 analyses were conducted; however, clear group clustering was unsuccessful. We also
154 investigated time-resolved lipidome remodeling in DKO vs. DKO control mice through
155 standard univariate analysis. For each lifetime stage, the number of significant lipid features
156 was identified (Welch's T -test P -value < 0.05). Fourteen lipids were significant in lifetime
157 stage I, 121 in lifetime stage II, 56 in lifetime stage III, 136 in lifetime stage IV, and 298 in
158 lifetime stage V (**Figure 2c**). There was a progressive increase in the number of significantly
159 altered lipids as HGSC advanced, except for the observed decrease from lifetime stage II to
160 III. This overall temporal trend seems to mimic HGSC evolution in humans where the
161 disease evolves from an asymptomatic early stage with only minimal metabolic changes to
162 being more easily detectable at more advanced stages where profound metabolic changes
163 are expected. A breakdown for the significant lipids common across stages is presented in
164 the upset plot in **Figure 2d**. A total of 71.4 % of the lipids were unique to lifetime stage I,
165 48.8 % to stage II, 46.4 % to stage III, 44.8 % to stage IV, and 68.1 % to stage V.
166 Furthermore, a total of 19 serum lipids were found to be significantly altered in at least three
167 of the five lifetime stages (**Table S2**). Of these, 68.4 % were PC or PC-O, making these the
168 most upregulated lipid classes based on univariate time-resolved analysis.

169 **Lipidome alterations in response to ovarian cancer progression.**

170 Taking advantage of the granularity of our longitudinal RP UHPLC-MS dataset, we
171 investigated lipidome changes associated with OC progression by identifying lipid
172 trajectory clusters and calculating pairwise correlations between lipids in each cluster
173 (**Figure 3, Table 1**). The dataset consisting of 87 significant lipids (Welch's T -test, BH q -
174 value < 0.05 , DKO vs. DKO mice) was used for this analysis. To study the temporal
175 evolution of these lipid alterations, time-resolved average lipid abundances in DKO and
176 DKO control mice were computed. Using fold changes between the average lipid
177 abundances ($\text{Log}_2[\text{DKO/control}]$), hierarchical clustering was used to identify four main
178 lipid trajectory clusters (A-D). In cluster A, the lipid fold changes increased in DKO mice
179 from lifetime stage I to II, decreased from II to III, and then spiked back up in V. Similar
180 temporal trends were observed for cluster B lipids. However, in cluster C, lipids increased
181 from lifetime stage I to II, decreased from II to III, and increased back from III to IV,
182 followed by a mostly slight downward trend from lifetime stage IV to V. Finally, cluster D
183 lipids had a relatively mild temporal change from lifetime stage I to IV, with a sharp increase
184 from IV to V (**Figure 3a-b**). A correlation network graph for these clusters is presented in
185 **Figure 3c**, showing the connectivity of related and the same lipid classes. A common
186 characteristic of clusters A, B, and C was an increase of the specific lipids in DKO mice
187 from lifetime stage I to II, followed by a decrease in from stage II to III. These clusters were
188 mostly composed of ether-linked and ester phospholipids such as PC, PC-O, PE, PE-O, and
189

190 LPE. Of these lipid classes, PC and PC-O were the most represented, with 53.8% in cluster
191 A, 100% in cluster B, and 88.8% in cluster C. On the other hand, sphingolipids classes such
192 as HexCer and Cer comprised 79% of all cluster D lipid species. Significant serum lipidome
193 rewiring was apparent with disease progression as shown by clustering analysis, with mostly
194 PC and PC-O being perturbed at early stages and HexCer and Cer at advanced stages.

195 **Time-resolved machine learning discriminates tumor stages of HGSC in DKO mice.**

196 We subsequently employed in-depth machine learning (ML) to further characterize the five-
197 lifetime stages. The feature selection strategy in the ML computational pipeline (**Figure 4a**)
198 led to the selection of five lipid features for lifetime stage I, 25 for lifetime stage II, 18 for
199 lifetime stage III, 24 for lifetime stage IV, and 42 for lifetime stage V (**Table S3**). After
200 feature selection, five ML algorithms, including logistic regression, random forests (RF), *k*-
201 nearest neighbors (*k*-NN), support vector machine (SVM), and a voting classifier composed
202 of the four prior ML algorithms were used to discriminate DKO from DKO control mice
203 within each of the lifetime stages (**Figure 4a**). ML algorithms were trained under fivefold
204 cross-validation conditions, while a separate test set was used for testing purposes. Detailed
205 ML prediction results are presented in **Table S4**. For lifetime stage I (training set *n* = 43,
206 test set *n* = 19), RF, *k*-NN, and a voting classifier gave the best receiver operating curve area
207 under the curve (ROC AUC) test set score of 0.80 (**Figure 4b** and **g**). For lifetime stage II
208 (training set *n* = 60, test set *n* = 26), RF gave the highest ROC AUC test set score of 0.70
209 (**Figure 4c** and **g**). For lifetime stage III (training set *n* = 59, test set *n* = 26), logistic
210 regression had the highest ROC AUC test set score of 0.85 (**Figure 4d** and **g**). For lifetime
211 stage IV (training set *n* = 60, test set *n* = 26), RF gave the highest ROC AUC test set score
212 of 0.66 (**Figure 4e** and **g**), and finally, for lifetime stage V (training set *n* = 98, test set *n* =
213 42), SVM gave the highest score of 0.75 (**Figure 4f** and **g**).
214
215

216 Given that early detection of ovarian cancer is important for improving clinical outcomes,
217 an AUC value of 0.80 for the first-lifetime stage (0-30%) suggests the possibility of early
218 detection of OC *via* serum lipidomics, should the lipids in the panel also show significant
219 alterations in humans. The discriminant lipids included a medium-chain fatty acid, 3-
220 hydroxyphenyl-valerate, and four phospholipids: PE(O-34:3), PC(17:0_18:2), PC(38:6),
221 and PE(O-16:1_20:5) (**Figure 5a** and **Table S3**). Furthermore, the highest AUC value for
222 the five lifetimes was 0.85 for lifetime stage III (45-60%); the selected discriminant lipid
223 features included ester phospholipids PC(18:0_18:0), PC(16:0_20:4), PC(18:0_20:4),
224 PC(18:0_22:4), PC(37:6), and PI(18:1_20:4), ether phospholipids PE(O-18:0_18:2) and
225 PC(O-38:6), ceramides Cer(d33:1), Cer(d41:2), Cer(d45:1), cerebrosides HexCer(d38:0-
226 OH) and HexCer(d40:0) or HexCer(t42:0-OH), a fatty acid FA(18:2), a glycerol ester,
227 TG(18:0_18:1_18:2), prostaglandin A1, and a pyrimidine derivative (**Figure 5c**, **Table S3**).
228 Other selected lipid markers for lifetime stages II, IV, and V are shown in **Figures 5b**, **d**, **e**,
229 and **Table S3**. A summary of the lipid categories represented in each of the ML discriminant
230 panels is given in **Figure 5f**. Phospholipids were the most represented category in all the
231 five lipid discriminant panels. Of all the phospholipid classes, PC and PC-O were the most
232 abundant species. The least represented lipid category was steroid lipids, with just one
233 cholesterol derivative selected in the lifetime stage V (75-100%) panel. Furthermore, of all
234 the lipids selected as markers, only phospholipids and fatty acyls (composed mostly of fatty
235 acids) were selected in all the lifetime stages. In summary, the early progression of OC was
236 marked by increased levels of phospholipids, notably PC and PC-O while, in contrast, later
237 stages were marked by more diverse lipids alterations, including sphingolipids, fatty acyls,
238 glycerolipids, steroid lipids, and phospholipids. Apart from phospholipids, sphingolipids
239 were the most represented lipid category at stages IV and V, consisting of mostly HexCer,

240 Cer, and SM (**Figure 5f**). These results agree with the lipid trajectory clustering results
241 discussed earlier.

242 **Prognostic circulating lipids in DKO mice**

243 Because prognostic makers are useful in providing information on the likely health outcome
244 of cancer patients, we employed survival analysis methods to investigate lipid species
245 predictive of the course of OC in DKO mice. First, candidate lipids were selected by
246 comparing all 1070 lipid features in DKO lifetime stages II – V with DKO lifetime stage I.
247 Lipids features with p -values < 0.05 (Welch's T -test) and at least one fold change (\log_2FC ,
248 DKO lifetime stage II-V vs. DKO stage I) were selected, resulting in a set of ten different
249 lipids in DKO lifetime stages I vs. II (**Figure 6a**), 56 in I vs. III (**Figure 6b**), 68 in I vs. IV
250 (**Figure 6c**), and 29 in I vs. V (**Figure 6d**). A breakdown of overlapping and unique lipid
251 features in these subsets is given in the upset plot in **Figure 6e**. A total of 12 lipids were
252 present in at least three sets from various lifetime pair comparisons. These lipids were
253 selected as prognostic candidates (**Figure 6e**). Furthermore, the 19 lipid features found to
254 be differential in at least three of the five lifetime stages (**Figure 2d**) were also selected as
255 candidate prognostic lipids. All fifteen DKO animals were binned into two groups based
256 on a median split using all 31 candidate prognostic lipids. A DKO 'Low' group was built
257 from mice with lipid abundances lower than or equal to the median of the relative
258 abundances of the selected lipids, while mice with abundances greater than the median were
259 bundled into a DKO 'High' group. Three lipid species of the 31 lipid candidates had a
260 statistically significant difference in their Kaplan Meier (KM) curves *via* the log-rank test.
261 These included PC(39:4) (p -value = 0.003, **Figure 6f**), PC(37:2) (p -value = 0.02, **Figure**
262 **6g**), and PC(40:7) (p -value = 0.008, **Figure 6h**). Of the 3 prognostic lipids, PC(39:4) had
263 the strongest prognostic effects with an $\Delta RMST$ of 10.96, followed by PC(40:7) ($\Delta RMST$
264 = 9.35), and then PC(37:2) ($\Delta RMST$ = 7.75) (**Figure S3**). All the prognostic circulating
265 lipids had elevated levels in DKO mice compared to DKO control mice for all time points
266 combined (**Figure 6h**).
267
268

269 **Discussion**

270 Given that most metabolomic cancer studies are based on a snapshot of the metabolic
271 process (14-18), it is not surprising that an understanding of the metabolic pathogenesis of
272 HGSC remains elusive. In this study, we performed nontargeted serum lipidomics of DKO
273 mice, an ovarian HGSC mouse model. We examined the temporal interplay of serum lipids
274 in ovarian HGSC progression. Ovarian HGSC originates in the fallopian tube where
275 fallopian tube epithelial (FTE) cells may be transformed into serous tubal intraepithelial
276 carcinoma (STIC) lesions. STIC metastasize into the ovary and then to the omentum (20).
277 The omentum, an extensive network of adipose tissue, provides a secondary metastasis hub
278 (21, 22), further underscoring the importance of investigating ovarian HGSC pathogenesis
279 through lipidome alterations. Reassuringly, our study identified similarly altered lipids as a
280 previous study at a fixed time point (19), validating the experimental approach applied here.
281 As expected, and given the pathogenesis of HGSC (20), significant lipid alterations were
282 evident from the data analysis performed when all time points were combined. The most
283 altered lipid classes at a global level included sphingolipids and phospholipids, with the
284 general trend showing that the number of significant lipids for each lifetime stage increased
285 as ovarian HGSC progressed. PC and PC-O were the most perturbed lipid classes, following
286 perturbations shown in previous metabolomic studies (23).
287
288

288 **Phospholipids**

289 Phospholipids, specifically ether and ester phospholipids, are by far the predominant lipid
290 classes present in clusters A-C of the temporal trend analyses conducted in this study, with
291 PC and PC-O being the key lipid families. This finding is not surprising, as PC comprise
292 approximately 40-50% of all total cellular phospholipids (24). Furthermore, cancer cells
293 require increased generation and maintenance of cellular membranes, largely composed of
294 phospholipids (25). Iorio *et al.* reported the activation of phosphatidylcholine-cycle
295 enzymes in human epithelial ovarian cancer (EOC) cells (26). In that study, the authors
296 reported increased phosphocholine (Pcho) levels and upregulation of choline kinase
297 (ChoK)-mediated phosphorylation, providing a plausible explanation for the observed
298 increase in PC levels, particularly for the progression from lifetime stage I to II in clusters
299 A-C. These data strongly suggest upregulation of the Kennedy pathway (27), with a
300 predominance of PC generation. Altered PC levels in ovarian cancer have been previously
301 reported in human studies (28) and in an ovarian cancer mouse model (23). This temporal
302 trend for phospholipids agrees with the discriminant lipids selected for DKO classification
303 tasks for all lifetime stages (Figure 5f). PCs and PC-Os comprise most of the lipids selected
304 for classification within lifetime stage II. In addition, phospholipids have the highest
305 percentage of discriminant lipids at all lifetime stages, with a decreasing proportion as
306 HGSC progresses. This finding suggests that phospholipids may play lesser roles in
307 advanced HGSC. In addition, three PC species (PC(39:4), PC(37:2), and PC(40:7)) were
308 identified as potential prognostic circulating lipids.

309
310 Of all discriminant lipids identified, most phospholipids species increased, while a few
311 decreased, such as LPE and LPC. LPC perturbations have been reported in an ovarian cancer
312 human study (28) and LPE species have been suggested as early-stage ovarian cancer
313 biomarkers in another human study (14). In a study of the triple knock out (TKO) HGSC
314 mouse model, LPE and LPC were likewise altered (23). In our study, LPE(18:1),
315 LPC(20:4/0:0), and LPC(20:5/0:0) were selected as discriminant lipids for lifetime stage V,
316 with decreased levels in DKO mice. LPC and LPE are the first step in Land's cycle, the
317 biochemical pathway involved in the remodeling of PC and PE (29). LPC and LPE are
318 mainly derived from partial hydrolysis of PC and PE, respectively, *via* phospholipase A₁
319 and A₂ (PLA₁ & PLA₂) (30). Decreased relative abundances of these lipid classes at lifetime
320 stage V can be explained by the sustained upregulation of PC and PE. Indeed, longitudinal
321 lipidome analysis of the TKO mouse model showed that most LPC species were lower in
322 abundance and most PC species much higher in HGSC (23). Furthermore, in a large-scale
323 profiling study of metabolic dysregulation in human ovarian cancer, LPC and LPE were
324 reported to be elevated in localized epithelial ovarian cancer (EOC) and downregulated in
325 metastatic EOC (31). These results align with findings for lifetime stage V for LPE and
326 LPC.

327
328 Another class of phospholipids that emerged as important were the phosphatidylinositols
329 (PI). These lipids are the central actors in the PI and PIP₂ cycles underpinning several
330 mammalian cell signaling pathways (32). There, PI is converted into phosphatidylinositol-
331 4-phosphate (PI4P), which is further converted into phosphatidylinositol-4,5-bisphosphate
332 (PIP₂) *via* various phosphokinases. PIP₂, on the other hand, is a component of the
333 phosphatidylinositol 3-kinase (PI3K) pathway that has been extensively implicated in
334 cancer (33). PI3Ks are lipid kinases that phosphorylate PIP₂ at the 3-OH inositol group to
335 yield phosphatidylinositol 3,4,5-trisphosphate (PIP₃). PIP₃ activates the serine/threonine
336 protein kinase, which plays a key role in carcinogenesis (33). The perturbation of PI levels
337 in HGSC can be rationalized by increased phosphatidylinositol 3-kinase (PI3-kinase)
338 activity, due to the increased copy numbers of the p110 α catalytic subunit of the enzyme in

339 ovarian cancer (34). This altered signaling pathway has been linked to cell proliferation
340 (35), glucose metabolism (36), and various types of oncogenic transformations (37). In
341 addition, alteration of PI levels has been reported in a DKO lipidomic study (19), and
342 proposed as a potential trait of early-stage OC in humans (14).

343 **Sphingolipids**

344 Cluster D in the hierarchical clustering temporal analysis results (**Figure 3**) consists mainly
345 of ceramides (Cer) and hexosylceramides (HexCer) with a characteristic abundance spike
346 from lifetime stage IV to V (*i.e.*, towards the end of the animal's life cycle). Ceramides are
347 essential intermediates in sphingolipid metabolism, acting as substrates for more complex
348 sphingolipids or degradation products. For example, HexCer and sphingomyelins (SM) are
349 derived from Cer, while SM and HexCer can be degraded to Cer by sphingomyelinases
350 (SMAse) and cerebrosidases, respectively. Altered sphingolipid metabolism has been
351 implicated in leukemia (38), hepatocellular (39), colorectal (40) and ovarian cancers (41).
352 Long-chain ceramides have been identified as possible diagnostic biomarkers of human
353 epithelial ovarian cancer (41). Sphingolipid metabolism has also been implicated in
354 regulating autophagy (42). Autophagy's primary role is to regulate cellular homeostasis by
355 removing damaged organelles and aggregated proteins; however, under high-stress
356 conditions, such as nutrition starvation, autophagy contributes to maintaining cellular
357 functions by supplying energy to the cell (43). As such, in the early cancer stages, autophagy
358 possesses an anti-carcinogenic function by attempting to maintain normal cellular
359 operations (43). On the other hand, at the late stages of cancer development, autophagy
360 confers tumor cell survival functions to counteract metabolic stress (44), directly explaining
361 the temporal trends of lipids in cluster D. As such, the role of autophagy in cancer can be
362 said to be paradoxical. Furthermore, ceramide glycosyltransferases, an enzyme class that
363 catalyzes the formation of hexosylceramides, has been implicated in playing a role in tumor
364 progression (45). Overexpression of uridine diphosphate-glucose ceramide
365 glucosyltransferase (UGCG), the gene involved in the synthesis of glucosylceramide, has
366 also been reported in ovarian cancer cells (45). The highest abundance increase for a
367 discriminant lipid was for HexCer(d34:1) in lifetime stage V. Finally, five SM species were
368 selected in the lifetime stage V classification task, all having low relative abundances in
369 DKO mice *vs.* DKO controls. In contrast, cluster D lipids showed overwhelmingly increased
370 levels of Cer and HexCer at the late stages. This metabolic trend suggests a conversion of
371 SM to Cer via SMAse to sustain the continued proliferative effects of Cer in tumor cells.
372

373 **Fatty Acids, Triglycerides and Other Derivatives**

374 Cancer cells can shunt energy from glucose into fatty acid synthesis (46), and the metabolic
375 rearrangements are pivotal in cell signaling and tumor growth (47). The observed alterations
376 in fatty acids abundances at every single lifetime stage examined are a result of this
377 metabolic shift. Enzymes associated with lipid syntheses, such as acetyl-CoA carboxylase
378 (ACC) and ATP-citrate lyase (ACL), are overexpressed and involved in tumorigenesis in
379 various tumors cell types (48-50). Fatty acid synthase (FAS), a multi-enzyme protein whose
380 main role is to synthesize palmitate from acetyl-CoA and malonyl-CoA, has also been found
381 to be upregulated in ovarian cancer tissues and associated with poor disease prognosis (51).
382 Furthermore, stearoyl-CoA desaturase-1 (SCD1), the enzyme that catalyzes the production
383 of saturated fatty acids from mono-unsaturated fatty acids, is upregulated in ovarian cancer
384 stem cells (52). Exogenous fatty acid metabolism also plays a role in ovarian cancer
385 development (46). For instance, fatty acid binding protein (FABP4) has been identified at
386 the interface of adipocytes and ovarian tumor cells in omental metastases (53). Furthermore,
387 CD36, a member of the fatty acid transport proteins (FATP), a transmembrane transport
388

389 protein that allows long-chain fatty acids into the cells, has also been implicated in breast
390 cancer progression and metastasis (54). Our ML algorithm selected FA species as
391 discriminant across all lifetime stages. Five of these were decreased in DKO mice relative
392 to controls. These species included 3-hydroxyphenyl-valerate, FA(26:1), and FA(18:3).
393 Changes in FA levels during tumor development most likely indicate the interplay between
394 FA synthesis and FA cell uptake, concomitant with FA metabolism associated with the
395 synthesis of complex lipids.

397 Estrogens, whose significant roles in the development and metastasis of ovarian cancer are
398 well-documented (55), have been linked to increased levels of TG in mice (56) and humans
399 (57, 58). This provides a biological link between estrogens and TG in ovarian cancer
400 pathogenesis. Furthermore, in a metabolic study involving over a hundred thousand subjects
401 and a ten-year follow-up period, serum TG were shown to positively correlate with
402 gynecological (ovarian, endometrial, cervical) cancer risk (59). In our study, TG(60:12) was
403 selected as one of the cluster A lipids, with levels spiking up from lifetime stage I to II,
404 decreasing from II to III, and then increasing in stages IV and V. In addition, two
405 triglycerides, TG(56:9) and TG(58:9), belong to cluster D lipids which have a characteristic
406 spike from lifetime stages IV to V. For ML classification tasks, most TG played a
407 discriminatory role in lifetime stage V, with 8 out of 9 having higher relative abundance in
408 DKO mice. A serum metabolomics study comparing DKO mice with controls also found a
409 triglyceride (TG 55:7) that increased in DKO mice (19). Triglycerides are used for energy
410 storage, which is very much needed to support cell growth as cancer progresses. This
411 suggests the upregulation of the monoacylglycerol and glycerol phosphate pathways.

412
413 Other selected discriminant lipids included prostaglandin A1 (PGA1), an eicosanoid. This
414 lipid was lower in DKO mice in the third lifetime stage. Higher abundances of prostaglandin
415 and prostaglandin D2 have been found to inhibit human ovarian cancer cell growth both *in*
416 *vitro* and in mice (60). Similarly, A-class prostaglandins are known to have antiproliferative
417 effects by blocking the cell cycle and activating apoptotic cascades (61). A cholesterol
418 derivative was also selected as a discriminant lipid in lifetime stage V, with an increased
419 abundance in DKO mice. Cholesterol metabolites have been linked to the promotion of
420 tumorigenesis (62). Furthermore, high serum cholesterol level has been linked to increased
421 ovarian cancer risk in a prospective study (63).

422 423 **Conclusions**

424 We here present a deep temporal lipidomic study of an HGSC ovarian cancer mouse model.
425 The main findings are summarized in **Figure 7**, pointing at numerous alterations in a variety
426 of lipid pathways. Phospholipids were the most perturbed lipid class. They also represented
427 the highest number of altered species at the early stages of HGSC development, pointing to
428 cell integrity fortification processes associated with cancer progression. We also found that
429 ceramide and hexosylceramide levels predominantly increased in DKO mice at the later
430 stages of OC progression. It is well known that sphingolipid metabolism is linked to cancer
431 development and progression via autophagy. In the early stages, an attempt is made to
432 inhibit tumorigenesis; however, at later stages, those lipids assist in cancer proliferation.
433 Furthermore, we identified sets of lipids that discriminate between DKO and DKO control
434 mice, even at the earliest stages of disease progression. In addition, three phospholipid
435 species were identified as circulating prognostic markers in DKO mice. These findings
436 underscore the potential for the existence of early-stage diagnostic or prognostic lipid
437 biomarker panels for human ovarian cancer.

Materials and Methods

Experimental Design

Dicer^{flox/flox} *Pten*^{flox/flox} *Amhr2*^{cre/+} DKO females and *Dicer*^{flox/flox} *Pten*^{flox/flox} control females that do not carry *Amhr2*^{cre/+} were generated, with the genotypes confirmed by PCR amplification of DNA. Mice were housed in the Baylor College of Medicine vivarium in dedicated mouse rooms in microisolator cages. When animals reached eight weeks of age, serum samples were collected from mice every two weeks until the end of the study or humane endpoint for sacrifice. When a DKO mouse with an advanced-stage cancer was determined to be severely sick, the mouse was anesthetized for the last blood collection via cardiac puncture, and euthanized. The submandibular vein was chosen for the serial blood collection by alternating cheek sides following a valid animal protocol (AN-716). A total of 100-200 µl blood sample was collected into a BD serum separator, allowed for 30 minutes clotting time, and followed by centrifugation and serum collection. Collected serum samples were stored at -80 °C for further metabolomics analysis. DKO mice were sacrificed for this study in accordance to the animal protocol approved by the institutional animal Care and Use Committee (IACUC) at Baylor College of Medicine. Samples from 15 DKO mice ($n = 231$) and 15 control mice ($n = 238$) were used for lipidomics analyses. Prior to data analysis, timepoints for each sample collected were converted into a percentage lifetime metric with the following mathematical formula:

$$\% \text{ Lifetime} = \frac{\text{Age of mice (weeks)}}{\text{Total lifespan of mice (weeks)}} \times 100$$

The % lifetimes were then binned into five categories: 0-30% (stage I), 30-45% (stage II), 45-60% (stage III), 60-75% (stage IV), and 75-100% (stage V).

Reagents

Optima LC-MS grade water, 2-propanol, acetonitrile, formic acid (99.5+%), ammonium formate, and ammonium acetate were purchased from Fisher Chemical (Fisher Scientific International, Inc. Pittsburgh, PA) and used to prepare chromatographic mobile phases and solvents for extraction. Isotopically labeled lipid standards (Table S5) were purchased from Avanti Polar Lipids (Alabaster, AL) and used to prepare the lipid internal standard mixture.

Sample Preparation

The lipid extraction solvent was prepared by adding 700 µL of the isotopically labeled lipid standard mixture (Table S5) to 42 mL of 2-propanol. Serum samples were thawed on ice, followed by the extraction of non-polar metabolites. The extraction procedure was carried out by adding the prepared extraction solvent to 10-25 µL serum sample in a 3:1 ratio. Following this step, samples were vortex-mixed for 30 s and centrifuged at 13,000 rpm for 7 min. The supernatant was transferred to LC vials and stored at -80 °C until analysis, which was performed within a week. A blank sample, prepared with LC-MS grade water, underwent the same sample preparation process as the serum samples. A pooled quality control (QC) sample was prepared by adding 2-5 µL aliquot of supernatant to each serum sample. This QC sample was analyzed every 10 injections to assess LC-MS instrument stability through the course of the experiment. Samples were run in a randomized order on consecutive days.

UHPLC-MS Analysis

Reverse-phase (RP) ultra-high performance liquid chromatography-mass spectrometry (UHPLC-MS) analysis was performed with a Thermo Accucore C30, 150 × 2.1 mm, 2.6 μm particle size column mounted in a Vanquish LC coupled to an Orbitrap ID-X Tribrid mass spectrometer (ThermoFisher Scientific). The mobile phases and chromatographic gradients used are described in Supplementary Table S6. MS data were acquired in positive and negative ion modes in the 150-2000 *m/z* range with a 120,000 mass resolution setting. The most relevant MS parameters are provided in the supplementary section Table S7. Samples were kept at 4 °C in the autosampler during LC-MS analysis while the column temperature was set to 50 °C. An injection volume of 2 μL was used for all runs. For lipid annotation, MS/MS experiments were performed using the Thermo Scientific AcquireX data acquisition workflow. Tandem MS data were acquired at a resolution of 30,000 and an isolation window of 0.4 *m/z*. Precursor ions were fragmented with HCD and CID activation methods. For HCD, stepped normalized collision energy (NCE) of 15, 30, and 45 and a CID collision energy of 40 were used to fragment the precursor ions.

UHPLC-MS Data Processing

Spectral features (described as *m/z*, retention time pairs) were extracted with Compound Discoverer v3.2 (ThermoFisher Scientific) from the raw files. This procedure included retention time alignment of chromatographic peaks, peak picking, peak area integration, and compound area correction using a QC-based regression curve. The sample blank injection was used to remove background peaks: features with less than five times the peak area of corresponding features in the sample blank were marked as background signals and removed from the dataset. Additionally, features that were not present in at least 50% of the QC sample injections or had a relative standard deviation (RSD) of more than 30% in the QC injections were removed from the dataset.

Lipid Annotation

Lipid annotation was conducted for selected spectral features detected following filtering. The exact masses and MS/MS spectra of all features were first matched against a curated in-house lipid spectral database. For features of interest that did not have matches in the local database, the generated elemental formulas, exact masses, and MS/MS spectra were matched against databases such as Lipid Maps (64) and mzCloud (65). A total of 1070 species, which included fatty acids, glycerophospholipids, sphingolipids, and glycerolipids, were successfully annotated with this approach and used for further analysis. The complete dataset of annotated species is available through the Metabolomics Workbench, as described above.

Global Lipidome Analysis

To investigate alterations at the lipidome level, fold changes were computed by taking the base two logarithmic ratio of the lipid abundances for DKO mice to the DKO control mice ($\log_2 \frac{[\text{DKO}]}{[\text{control}]}$). Statistically significant lipids were identified *via* Welch's *T*-test (DKO *n*=221, DKO control *n*=238) followed by a Benjamini-Hochberg correction using the Statsmodel library (v. 0.12.2). Eighty-seven lipids with *q* < 0.05 were identified as significant. These lipids features were log-transformed ($\log_2 X$) and auto-scaled prior to unsupervised machine learning. Principal component analysis (PCA), kernel PCA (kPCA), and t-distributed stochastic neighbor embedding (t-SNE) were performed with the sci-kit learn library (v. 0.24.1). In addition, uniform manifold approximation and projection (UMAP) were performed using the umap library (v. 0.5.1). A two-step pipeline was set up to identify the best hyperparameters for kPCA. First, a kPCA dimensionality reduction to the first two components, followed by a logistic regression classifier, then GridSearchCV

in the sci-kit learn library was used to select the best kernel and gamma value for the algorithm. The gamma value selected was 0.03, while the kernel used was the radial basis function (RBF). For t-SNE, the following hyperparameters were used: perplexity= 4, early exaggeration=10. Perplexity controls how the balance between the local and global structure of the data, while early exaggeration is the factor that increases the attractive forces between data points. Time-resolved lipid changes were computed by comparing the five lifetime stages of DKO and DKO control mice with a Welch's *T*-test. Lipids with $p < 0.05$ were identified as significant. In addition, overlapping significant features in the time-resolved univariate test were identified using an upset plot library (v. 0.6.0). Significant lipids that appeared in at least three lifetime stages were screened as potential prognostic circulating lipids for ovarian cancer.

Lipidome Longitudinal Analysis

Fold changes, as described above, were computed for 87 lipids with $q < 0.05$, and hierarchical clustering analysis (HCA) was then used to identify clusters of lipidomic trajectories using those fold changes. Each row of the dataset is equivalent to the fold change values over the five lifetime stages for a given lipid feature. The goal of this analysis was to cluster lipids that have a similar trend over time. HCA was performed using the SciPy library (v. 1.6.2). The distance hyperparameter, that is the distance between two observations (lipids), used was the correlation metric, which is defined as follows:

$$1 - \frac{(x - \hat{x}) \cdot (y - \hat{y})}{\|x - \hat{x}\|_2 \|y - \hat{y}\|_2}$$

Where x and y are two lipid features.

The second hyperparameter, the linkage hyperparameter, is the measure of the distance between two clusters to be merged. Complete linkage was used – this method computes the maximum distance between any single data point in the first cluster and any single data point in the second cluster, which is defined as follows:

$$D(X, Y) = \max_{x \in X, y \in Y} d(x, y)$$

The algorithm then fuses clusters that have the shortest distance between each other. Where $d(x, y)$ is the distance between lipids $x \in X$ and $y \in Y$ and X and Y are two sets of lipid clusters. Four lipid clusters were identified to have biologically meaningful trends over time. The longitudinal lipid changes of the four lipid clusters were visualized using the HoloView Python library (v. 1.14.6). The correlation network graphs of the four clusters were plotted using Plotly (v. 5.3.1) and networkX (v. 2.5). Lipids with $r \geq 0.5$ (Pearson's correlation coefficient) are displayed with a link on the network graphs.

Machine Learning Classification Methods

Feature selection

For each lifetime stage, only lipid features with P values < 0.05 (Welch's *T*-test) were retained. Furthermore, one feature was retained for every two highly correlated lipid features (Pearson's correlation, $r > 0.8$). Samples were divided into a training set (70% of total samples) and a test set (30% of total samples). Lipid features were selected by fitting the training datasets with a meta-transformer for selecting features based on importance weights. In this case, random forests were used, and features were ranked *via* their Gini index feature importance score. The features with a Gini index greater or equal to the mean

of all Gini indices were the final lipid features selected for classification purposes. The number of trees used for the random forest classifiers was a hundred, and all samples were autoscaled prior to feature selection with random forests. Feature selection was carried out with the SelectFromModel function and Random Forest classifier in the sci-kit learn library (v. 0.24.1).

ML algorithms

Classification tasks were performed by training machine learning models to discriminate DKO from DKO control mice using the features selected as described above. The machine learning algorithms used included logistic regression, random forest, k -nearest neighbors, support vector machines, and a voting ensemble classifier. The default parameters of Python's sci-kit learn machine learning library (v. 0.24.1) were used. As indicated above, 70% of samples were used for training purposes, with a 5-fold cross-validation method, while the remaining 30% were used as the test set. The classifiers were evaluated using the area under the curve of the receiver operating characteristic curve (AUC ROC) metric. ROC is a probability curve that plots the true positive rate (TPR) against the false positive rate (FPR) at various threshold values. This feature makes it an unbiased metric score, particularly for an unbalanced dataset.

Logistic regression

Logistic regression is a regression algorithm used for classification purposes, in this case, binary classification (DKO vs. DKO control mice). It is an extension of linear regression, as it computes a weighted sum of input features in addition to a bias term. However, instead of outputting a numeric value as in linear regression, the numeric value is passed through a sigmoid function that computes a probability (\hat{p}) value between 0 and 1.

$$\hat{y} = \sigma(wx + b)$$

Where $\sigma(\cdot)$ is the logistic function, \mathbf{w} is the weights/vector coefficient, x is lipid features, \mathbf{b} is the bias term, and \hat{y} is the final prediction. \mathbf{w} and \mathbf{b} are the parameters set during training and are used to classify samples of the test sets. Probability values are stratified as described below:

$$\hat{y} = \begin{cases} 0 & \text{if } \hat{p} < 0.5 \\ 1 & \text{if } \hat{p} \geq 0.5 \end{cases}$$

In our case, samples with $\hat{p} < 0.5$ were classified as control animals, while $\hat{p} \geq 0.5$ were classified as DKO animals.

Random forest classification

Random forests are an ensemble of decision trees. A decision tree takes the form of an inverted tree, starting with a root node at the top, with the node split by lipid features into internal nodes, culminating with the leaf node. While lipid features split each node, as indicated, the leaf nodes give the final classification of either DKO or DKO control mice. Decision trees are assembled to form the random forest via bootstrap aggregation, which reduces prediction variance by random sampling of training samples with replacement. The algorithm also introduces additional randomness during tree construction by using a random subset of features to search for the best features to split the node, resulting in greater tree diversity. For this work, the number of trees in the forest is a hundred, and the quality of node split is measured by the Gini impurity.

Support vector machines

635 The goal of support vector machines (SVM) is to identify a separating hyperplane $\mathbf{b} + \mathbf{w}^T \mathbf{x}$
636 that will discriminate two classes of samples with the widest possible margins. Where \mathbf{w}
637 is the weights or coefficient vector, \mathbf{b} is the bias term, and \mathbf{x} is the feature value. This goal is
638 accomplished by learning the \mathbf{w} and \mathbf{b} terms during training with the following equation:

$$639 \quad \text{Min}_{\mathbf{w}, \mathbf{b}, \xi} \frac{1}{2} \|\mathbf{w}\|^2 + C \sum \xi, \text{ subj. to. } y(\mathbf{b} + \mathbf{w}^T \mathbf{x}) \geq 1 - \xi \text{ and } \xi \geq 0$$

641 Where C is a regularization parameter that penalizes or accommodates ξ , ξ is the slack
642 variable that allows for a soft margin classification, allowing some training data to fall
643 within the SVM margin. Therefore, the goal is to minimize the weights, bias, and slack
644 variables, subject to a correct prediction while accommodating the slack variables. In this
645 work, C was set to 1. A kernelized SVM was used to transform datasets that are not linearly
646 separable to a higher-dimensional space, where they may be linearly separable. The kernel
647 used in this work is the radial basis function kernel which is defined below:

$$648 \quad k(p, q) = e^{-\gamma \|p - q\|^2 + c}$$

649 Where p and q represent data points and γ is the kernel coefficient. After training, given a
650 test sample x , its prediction score can be obtained with OV score = $b + wx$. If the ovarian
651 cancer (OV) score ≤ 0 , the sample is classified as control mice, and vice-versa.

652 *k-Nearest Neighbors (k-NN)*

653 k-NN is a non-parametric supervised learning algorithm using an instance-based learning
654 method. It simply stores training data instances and computes votes based on the majority
655 class of the k nearest neighbors. The number of neighbors selected was five in this work,
656 and a uniform weight function was used. That is, all points in each neighborhood were
657 weighted equally.

658 *Voting classifier*

659 Because we selected machine learning models with different inductive biases, we explored
660 an ensemble method voting classifier. The estimators for the voting classifier include all the
661 ML models prior described: logistic regression, random forests, SVM, and k-NN. In
662 addition, soft voting was performed, using average predicted probabilities to predict class
663 labels.

664 **Prognostic Lipid Discovery Methods and Survival Analysis**

665 Feature selection was performed by a lifetime stage-resolved volcano plot analysis. This
666 involves plotting the $-\log_{10}P$ -value (Welch's T -test, DKO lifetime stages II-V vs. DKO stage
667 I) against the \log_2FC (Fold change, DKO lifetime stage II-V vs. DKO stage I). Lipid features
668 with P -values < 0.05 and at least one \log_2FC for each comparison pair were identified as
669 significant. Volcano plot analysis was performed using the Bioinfokit library (v. 2.0.8).
670 Overlapping significant features in the DKO volcano plot analysis were identified using an
671 upset plot via the Upset python library (v. 0.6.0). Lipids that were significant in at least three
672 of the four DKO lifetime stages comparisons were screened as potential prognostic
673 circulating lipids for ovarian cancer. In addition, significant lipids in at least three lifetime
674 stages comparison of DKO vs. control lifetime stages comparisons were also screened.

675 The selected lipids were used to split the DKO samples into two groups using the median
676 split method. For the last serum collection before mice death or end of the study, the DKO
677 samples with less than or equal to the median of the lipid's relative abundance were
678 designated as the "low metabolite level" group. In contrast, the DKO samples with greater
679

684 than the median of the lipid's relative abundance were designated the "high metabolite
685 level" group. Furthermore, the survival function $S(t) = P(T > t)$, which is the probability
686 that a mouse survives longer than some specified time t , was computed using the Kaplan
687 Meier (KM) estimate described in the equation below:
688

$$\hat{S}(t) = \prod_{t_i < t} \left(1 - \frac{d_i}{n_i}\right)$$

690 Where d_i is the number of mice death events at time t , while n_i is the number of mice at
691 risk of death prior to time t . The log-rank test ($p < 0.05$) was used to determine if the
692 differences between KM curves were statistically significant. In addition, the restricted
693 mean survival time (RMST) is defined below:
694

$$\text{RMST}(t) = \int_0^t S(\tau) d\tau$$

695
696
697 This metric was used to compare two survival curves by measuring the area under the
698 survival curve, which is a measure of "time lost." Kaplan Meier estimates and the RMST
699 was also used to compute and compare the survival curves of DKO vs. control mice,
700 respectively. Finally, the hazard curves were computed using the Nelson-Aalen estimate,
701 and all survival analysis methods in this work were performed using the Python lifelines
702 library (v. 0.26.3).
703
704

705 **Statistical Analysis**

706 Computational analysis was carried out as indicated in the respective sections above using
707 the Python 3.8.8 programming language. NumPy (v. 1.20.1) was used for numerical
708 computations, the Pandas (v. 1.2.4) library was used to perform data handling, and data
709 manipulation, Matplotlib (v. 3.3.4), Plotly (v. 5.3.1) and Holoview (v. 1.14.6) were used for
710 data plotting and visualization.
711
712
713

714 **References**

- 715 1. A. N. Giaquinto, R. R. Broaddus, A. Jemal, R. L. Siegel, The Changing Landscape of
716 Gynecologic Cancer Mortality in the United States. *Obstet Gynecol* **139**, 440-442 (2022).
- 717 2. M. Zou, Y. Du, R. Liu, Z. Zheng, J. Xu, Nanocarrier-delivered small interfering RNA for
718 chemoresistant ovarian cancer therapy. *Wiley Interdiscip Rev RNA* **12**, e1648 (2021).
- 719 3. L. A. Torre, B. Trabert, C. E. DeSantis, K. D. Miller, G. Samimi, C. D. Runowicz, M. M.
720 Gaudet, A. Jemal, R. L. Siegel, Ovarian cancer statistics, 2018. *CA Cancer J Clin* **68**, 284-
721 296 (2018).
- 722 4. E. Surveillance, and End Results (SEER) Program (www.seer.cancer.gov) SEER*Stat
723 Database. (National Cancer Institute, DCCPS, Surveillance Research Program, 2022).
- 724 5. M. A. Lisio, L. Fu, A. Goyeneche, Z. H. Gao, C. Telleria, High-Grade Serous Ovarian
725 Cancer: Basic Sciences, Clinical and Therapeutic Standpoints. *Int J Mol Sci* **20**, (2019).
- 726 6. J. Kim, E. Y. Park, O. Kim, J. M. Schilder, D. M. Coffey, C. H. Cho, R. C. Bast, Jr., Cell
727 Origins of High-Grade Serous Ovarian Cancer. *Cancers (Basel)* **10**, (2018).
- 728 7. J. Kim, D. M. Coffey, C. J. Creighton, Z. Yu, S. M. Hawkins, M. M. Matzuk, High-grade
729 serous ovarian cancer arises from fallopian tube in a mouse model. *Proc Natl Acad Sci U*
730 *SA* **109**, 3921-3926 (2012).

- 731 8. O. Kim, E. Y. Park, D. L. Klinkebiel, S. D. Pack, Y. H. Shin, Z. Abdullaev, R. E.
732 Emerson, D. M. Coffey, S. Y. Kwon, C. J. Creighton, S. Kwon, E. C. Chang, T. Chiang,
733 A. N. Yatsenko, J. Chien, D. J. Cheon, Y. Yang-Hartwich, H. Nakshatri, K. P. Nephew, R.
734 R. Behringer, F. M. Fernandez, C. H. Cho, B. Vanderhyden, R. Drapkin, R. C. Bast, Jr.,
735 K. D. Miller, A. R. Karpf, J. Kim, In vivo modeling of metastatic human high-grade
736 serous ovarian cancer in mice. *PLoS Genet* **16**, e1008808 (2020).
- 737 9. J. R. Cantor, D. M. Sabatini, Cancer cell metabolism: one hallmark, many faces. *Cancer*
738 *Discov* **2**, 881-898 (2012).
- 739 10. J. K. Nicholson, J. C. Lindon, Systems biology: Metabonomics. *Nature* **455**, 1054-1056
740 (2008).
- 741 11. K. Bingol, Recent Advances in Targeted and Untargeted Metabolomics by NMR and
742 MS/NMR Methods. *High Throughput* **7**, (2018).
- 743 12. M. I. Jordan, T. M. Mitchell, Machine learning: Trends, perspectives, and prospects.
744 *Science* **349**, 255-260 (2015).
- 745 13. O. O. Bifarin, D. A. Gaul, S. Sah, R. S. Arnold, K. Ogan, V. A. Master, D. L. Roberts, S.
746 H. Bergquist, J. A. Petros, F. M. Fernandez, A. S. Edison, Machine Learning-Enabled
747 Renal Cell Carcinoma Status Prediction Using Multiplatform Urine-Based Metabolomics.
748 *J Proteome Res* **20**, 3629-3641 (2021).
- 749 14. D. A. Gaul, R. Mezencev, T. Q. Long, C. M. Jones, B. B. Benigno, A. Gray, F. M.
750 Fernandez, J. F. McDonald, Highly-accurate metabolomic detection of early-stage ovarian
751 cancer. *Sci Rep* **5**, 16351 (2015).
- 752 15. E. I. Braicu, S. Darb-Esfahani, W. D. Schmitt, K. M. Koistinen, L. Heiskanen, P. Poho, J.
753 Budczies, M. Kuhberg, M. Dietel, C. Frezza, C. Denkert, J. Sehouli, M. Hilvo, High-grade
754 ovarian serous carcinoma patients exhibit profound alterations in lipid metabolism.
755 *Oncotarget* **8**, 102912-102922 (2017).
- 756 16. H. S. Ahn, J. Yeom, J. Yu, Y. I. Kwon, J. H. Kim, K. Kim, Convergence of Plasma
757 Metabolomics and Proteomics Analysis to Discover Signatures of High-Grade Serous
758 Ovarian Cancer. *Cancers (Basel)* **12**, (2020).
- 759 17. S. Plewa, A. Horala, P. Dereziński, E. Nowak-Markwitz, J. Matysiak, Z. J. Kokot, Wide
760 spectrum targeted metabolomics identifies potential ovarian cancer biomarkers. *Life Sci*
761 **222**, 235-244 (2019).
- 762 18. X. Wang, X. Zhao, J. Zhao, T. Yang, F. Zhang, L. Liu, Serum metabolite signatures of
763 epithelial ovarian cancer based on targeted metabolomics. *Clin Chim Acta* **518**, 59-69
764 (2021).
- 765 19. C. M. Jones, M. E. Monge, J. Kim, M. M. Matzuk, F. M. Fernandez, Metabolomic serum
766 profiling detects early-stage high-grade serous ovarian cancer in a mouse model. *J*
767 *Proteome Res* **14**, 917-927 (2015).
- 768 20. H. Lusk, J. E. Burdette, L. M. Sanchez, Models for measuring metabolic chemical changes
769 in the metastasis of high grade serous ovarian cancer: fallopian tube, ovary, and omentum.
770 *Mol Omics* **17**, 819-832 (2021).
- 771 21. R. S. Freedman, M. Deavers, J. Liu, E. Wang, Peritoneal inflammation - A
772 microenvironment for Epithelial Ovarian Cancer (EOC). *J Transl Med* **2**, 23 (2004).
- 773 22. J. Cai, H. Tang, L. Xu, X. Wang, C. Yang, S. Ruan, J. Guo, S. Hu, Z. Wang, Fibroblasts in
774 omentum activated by tumor cells promote ovarian cancer growth, adhesion and
775 invasiveness. *Carcinogenesis* **33**, 20-29 (2012).
- 776 23. S. Sah, X. Ma, A. Botros, D. A. Gaul, S. R. Yun, E. Y. Park, O. Kim, S. G. Moore, J. Kim,
777 F. M. Fernandez, Space- and Time-Resolved Metabolomics of a High-Grade Serous
778 Ovarian Cancer Mouse Model. *Cancers (Basel)* **14**, (2022).

- 779 24. J. N. van der Veen, J. P. Kennelly, S. Wan, J. E. Vance, D. E. Vance, R. L. Jacobs, The
780 critical role of phosphatidylcholine and phosphatidylethanolamine metabolism in health
781 and disease. *Biochim Biophys Acta Biomembr* **1859**, 1558-1572 (2017).
- 782 25. C. Stoica, A. K. Ferreira, K. Hannan, M. Bakovic, Bilayer Forming Phospholipids as
783 Targets for Cancer Therapy. *Int J Mol Sci* **23**, (2022).
- 784 26. E. Iorio, A. Ricci, M. Bagnoli, M. E. Pisanu, G. Castellano, M. Di Vito, E. Venturini, K.
785 Glunde, Z. M. Bhujwalla, D. Mezzanzanica, S. Canevari, F. Podo, Activation of
786 phosphatidylcholine cycle enzymes in human epithelial ovarian cancer cells. *Cancer Res*
787 **70**, 2126-2135 (2010).
- 788 27. F. Gibellini, T. K. Smith, The Kennedy pathway--De novo synthesis of
789 phosphatidylethanolamine and phosphatidylcholine. *IUBMB Life* **62**, 414-428 (2010).
- 790 28. R. J. Niemi, E. I. Braicu, H. Kulbe, K. M. Koistinen, J. Sehouli, U. Puistola, J. U.
791 Maenpaa, M. Hilvo, Ovarian tumours of different histologic type and clinical stage induce
792 similar changes in lipid metabolism. *Br J Cancer* **119**, 847-854 (2018).
- 793 29. V. B. O'Donnell, New appreciation for an old pathway: the Lands Cycle moves into new
794 arenas in health and disease. *Biochem Soc Trans* **50**, 1-11 (2022).
- 795 30. S. H. Law, M. L. Chan, G. K. Marathe, F. Parveen, C. H. Chen, L. Y. Ke, An Updated
796 Review of Lysophosphatidylcholine Metabolism in Human Diseases. *Int J Mol Sci* **20**,
797 (2019).
- 798 31. C. Ke, Y. Hou, H. Zhang, L. Fan, T. Ge, B. Guo, F. Zhang, K. Yang, J. Wang, G. Lou, K.
799 Li, Large-scale profiling of metabolic dysregulation in ovarian cancer. *Int J Cancer* **136**,
800 516-526 (2015).
- 801 32. F. Mazet, M. J. Tindall, J. M. Gibbins, M. J. Fry, A model of the PI cycle reveals the
802 regulating roles of lipid-binding proteins and pitfalls of using mosaic biological data. *Sci*
803 *Rep* **10**, 13244 (2020).
- 804 33. W. Zhao, Y. Qiu, D. Kong, Class I phosphatidylinositol 3-kinase inhibitors for cancer
805 therapy. *Acta Pharm Sin B* **7**, 27-37 (2017).
- 806 34. L. Shayesteh, Y. Lu, W. L. Kuo, R. Baldocchi, T. Godfrey, C. Collins, D. Pinkel, B.
807 Powell, G. B. Mills, J. W. Gray, PIK3CA is implicated as an oncogene in ovarian cancer.
808 *Nat Genet* **21**, 99-102 (1999).
- 809 35. A. Klippel, M. A. Escobedo, M. S. Wachowicz, G. Apell, T. W. Brown, M. A. Giedlin,
810 W. M. Kavanaugh, L. T. Williams, Activation of phosphatidylinositol 3-kinase is
811 sufficient for cell cycle entry and promotes cellular changes characteristic of oncogenic
812 transformation. *Mol Cell Biol* **18**, 5699-5711 (1998).
- 813 36. E. U. Frevert, B. B. Kahn, Differential effects of constitutively active phosphatidylinositol
814 3-kinase on glucose transport, glycogen synthase activity, and DNA synthesis in 3T3-L1
815 adipocytes. *Mol Cell Biol* **17**, 190-198 (1997).
- 816 37. H. W. Chang, M. Aoki, D. Fruman, K. R. Auger, A. Bellacosa, P. N. Tsichlis, L. C.
817 Cantley, T. M. Roberts, P. K. Vogt, Transformation of chicken cells by the gene encoding
818 the catalytic subunit of PI 3-kinase. *Science* **276**, 1848-1850 (1997).
- 819 38. M. W. Holliday, Jr., S. B. Cox, M. H. Kang, B. J. Maurer, C22:0- and C24:0-
820 dihydroceramides confer mixed cytotoxicity in T-cell acute lymphoblastic leukemia cell
821 lines. *PLoS One* **8**, e74768 (2013).
- 822 39. G. Grammatikos, N. Schoell, N. Ferreiros, D. Bon, E. Herrmann, H. Farnik, V. Koberle,
823 A. Piiper, S. Zeuzem, B. Kronenberger, O. Waidmann, J. Pfeilschifter, Serum
824 sphingolipidomic analyses reveal an upregulation of C16-ceramide and sphingosine-1-
825 phosphate in hepatocellular carcinoma. *Oncotarget* **7**, 18095-18105 (2016).
- 826 40. L. Chen, H. Chen, Y. Li, L. Li, Y. Qiu, J. Ren, Endocannabinoid and ceramide levels are
827 altered in patients with colorectal cancer. *Oncol Rep* **34**, 447-454 (2015).

- 828 41. N. Kozar, K. Kruusmaa, M. Bitenc, R. Argamasilla, A. Adsuar, N. Goswami, D. Arko, I.
829 Takac, Metabolomic profiling suggests long chain ceramides and sphingomyelins as a
830 possible diagnostic biomarker of epithelial ovarian cancer. *Clin Chim Acta* **481**, 108-114
831 (2018).
- 832 42. M. Dany, B. Ogretmen, Ceramide induced mitophagy and tumor suppression. *Biochim*
833 *Biophys Acta* **1853**, 2834-2845 (2015).
- 834 43. S. Sridhar, Y. Botbol, F. Macian, A. M. Cuervo, Autophagy and disease: always two sides
835 to a problem. *J Pathol* **226**, 255-273 (2012).
- 836 44. W. Jiang, B. Ogretmen, Autophagy paradox and ceramide. *Biochim Biophys Acta* **1841**,
837 783-792 (2014).
- 838 45. Z. Li, L. Zhang, D. Liu, C. Wang, Ceramide glycosylation and related enzymes in cancer
839 signaling and therapy. *Biomed Pharmacother* **139**, 111565 (2021).
- 840 46. H. Yoon, S. Lee, Fatty Acid Metabolism in Ovarian Cancer: Therapeutic Implications. *Int*
841 *J Mol Sci* **23**, (2022).
- 842 47. R. J. Deberardinis, N. Sayed, D. Ditsworth, C. B. Thompson, Brick by brick: metabolism
843 and tumor cell growth. *Curr Opin Genet Dev* **18**, 54-61 (2008).
- 844 48. G. Hatzivassiliou, F. Zhao, D. E. Bauer, C. Andreadis, A. N. Shaw, D. Dhanak, S. R.
845 Hingorani, D. A. Tuveson, C. B. Thompson, ATP citrate lyase inhibition can suppress
846 tumor cell growth. *Cancer Cell* **8**, 311-321 (2005).
- 847 49. K. Brusselmans, E. De Schrijver, G. Verhoeven, J. V. Swinnen, RNA interference-
848 mediated silencing of the acetyl-CoA-carboxylase-alpha gene induces growth inhibition
849 and apoptosis of prostate cancer cells. *Cancer Res* **65**, 6719-6725 (2005).
- 850 50. V. Chajes, M. Cambot, K. Moreau, G. M. Lenoir, V. Joulin, Acetyl-CoA carboxylase
851 alpha is essential to breast cancer cell survival. *Cancer Res* **66**, 5287-5294 (2006).
- 852 51. Y. Cai, J. Wang, L. Zhang, D. Wu, D. Yu, X. Tian, J. Liu, X. Jiang, Y. Shen, L. Zhang, M.
853 Ren, P. Huang, Expressions of fatty acid synthase and HER2 are correlated with poor
854 prognosis of ovarian cancer. *Med Oncol* **32**, 391 (2015).
- 855 52. U. V. Roongta, J. G. Pabalan, X. Wang, R. P. Ryseck, J. Fargnoli, B. J. Henley, W. P.
856 Yang, J. Zhu, M. T. Madireddi, R. M. Lawrence, T. W. Wong, B. A. Rupnow, Cancer cell
857 dependence on unsaturated fatty acids implicates stearoyl-CoA desaturase as a target for
858 cancer therapy. *Mol Cancer Res* **9**, 1551-1561 (2011).
- 859 53. K. M. Gharpure, S. Pradeep, M. Sans, R. Rupaimoole, C. Ivan, S. Y. Wu, E. Bayraktar, A.
860 S. Nagaraja, L. S. Mangala, X. Zhang, M. Haemmerle, W. Hu, C. Rodriguez-Aguayo, M.
861 McGuire, C. S. L. Mak, X. Chen, M. A. Tran, A. Villar-Prados, G. A. Pena, R.
862 Kondetimmanahalli, R. Nini, P. Koppula, P. Ram, J. Liu, G. Lopez-Berestein, K.
863 Baggerly, S. E. L, A. K. Sood, FABP4 as a key determinant of metastatic potential of
864 ovarian cancer. *Nat Commun* **9**, 2923 (2018).
- 865 54. Y. Liang, H. Han, L. Liu, Y. Duan, X. Yang, C. Ma, Y. Zhu, J. Han, X. Li, Y. Chen,
866 CD36 plays a critical role in proliferation, migration and tamoxifen-inhibited growth of
867 ER-positive breast cancer cells. *Oncogenesis* **7**, 98 (2018).
- 868 55. A. J. O'Donnell, K. G. Macleod, D. J. Burns, J. F. Smyth, S. P. Langdon, Estrogen
869 receptor-alpha mediates gene expression changes and growth response in ovarian cancer
870 cells exposed to estrogen. *Endocr Relat Cancer* **12**, 851-866 (2005).
- 871 56. H. J. Kim, R. K. Kalkhoff, Sex steroid influence on triglyceride metabolism. *J Clin Invest*
872 **56**, 888-896 (1975).
- 873 57. W. R. Hazzard, M. J. Spiger, J. D. Bagdade, E. L. Bierman, Studies on the mechanism of
874 increased plasma triglyceride levels induced by oral contraceptives. *N Engl J Med* **280**,
875 471-474 (1969).
- 876 58. T. O'Brien, T. T. Nguyen, Lipids and lipoproteins in women. *Mayo Clin Proc* **72**, 235-244
877 (1997).

- 878 59. H. Ulmer, W. Borena, K. Rapp, J. Klenk, A. Strasak, G. Diem, H. Concin, G. Nagel,
879 Serum triglyceride concentrations and cancer risk in a large cohort study in Austria. *Br J*
880 *Cancer* **101**, 1202-1206 (2009).
- 881 60. Y. Kikuchi, M. Miyauchi, K. Oomori, T. Kita, I. Kizawa, K. Kato, Inhibition of human
882 ovarian cancer cell growth in vitro and in nude mice by prostaglandin D2. *Cancer Res* **46**,
883 3364-3366 (1986).
- 884 61. B. Diez-Dacal, D. Perez-Sala, A-class prostaglandins: early findings and new perspectives
885 for overcoming tumor chemoresistance. *Cancer Lett* **320**, 150-157 (2012).
- 886 62. B. Huang, B. L. Song, C. Xu, Cholesterol metabolism in cancer: mechanisms and
887 therapeutic opportunities. *Nat Metab* **2**, 132-141 (2020).
- 888 63. K. J. Helzlsouer, A. J. Alberg, E. P. Norkus, J. S. Morris, S. C. Hoffman, G. W.
889 Comstock, Prospective study of serum micronutrients and ovarian cancer. *J Natl Cancer*
890 *Inst* **88**, 32-37 (1996).
- 891 64. E. Fahy, M. Sud, D. Cotter, S. Subramaniam, LIPID MAPS online tools for lipid research.
892 *Nucleic Acids Res* **35**, W606-612 (2007).
- 893 65. R. Mistrik, mzCLOUD: A spectral tree library for the Identification of "unknown
894 unknowns". *Abstracts of Papers of the 255th American Chemical Society National*
895 *Meeting*, (2018).
- 896
897
898
899
900
901
902

903 Acknowledgments

904
905 **Funding:** The authors acknowledge support through the National Cancer Institute
906 1R01CA218664-01 (FMF) for this project. M.P. is supported by NIH grant (R03
907 CA259664) and the Cancer Prevention Research Institute of Texas grant (RP220524). This
908 work was supported by Georgia Institute of Technology's Systems Mass Spectrometry
909 Core Facility.

912 Author contributions:

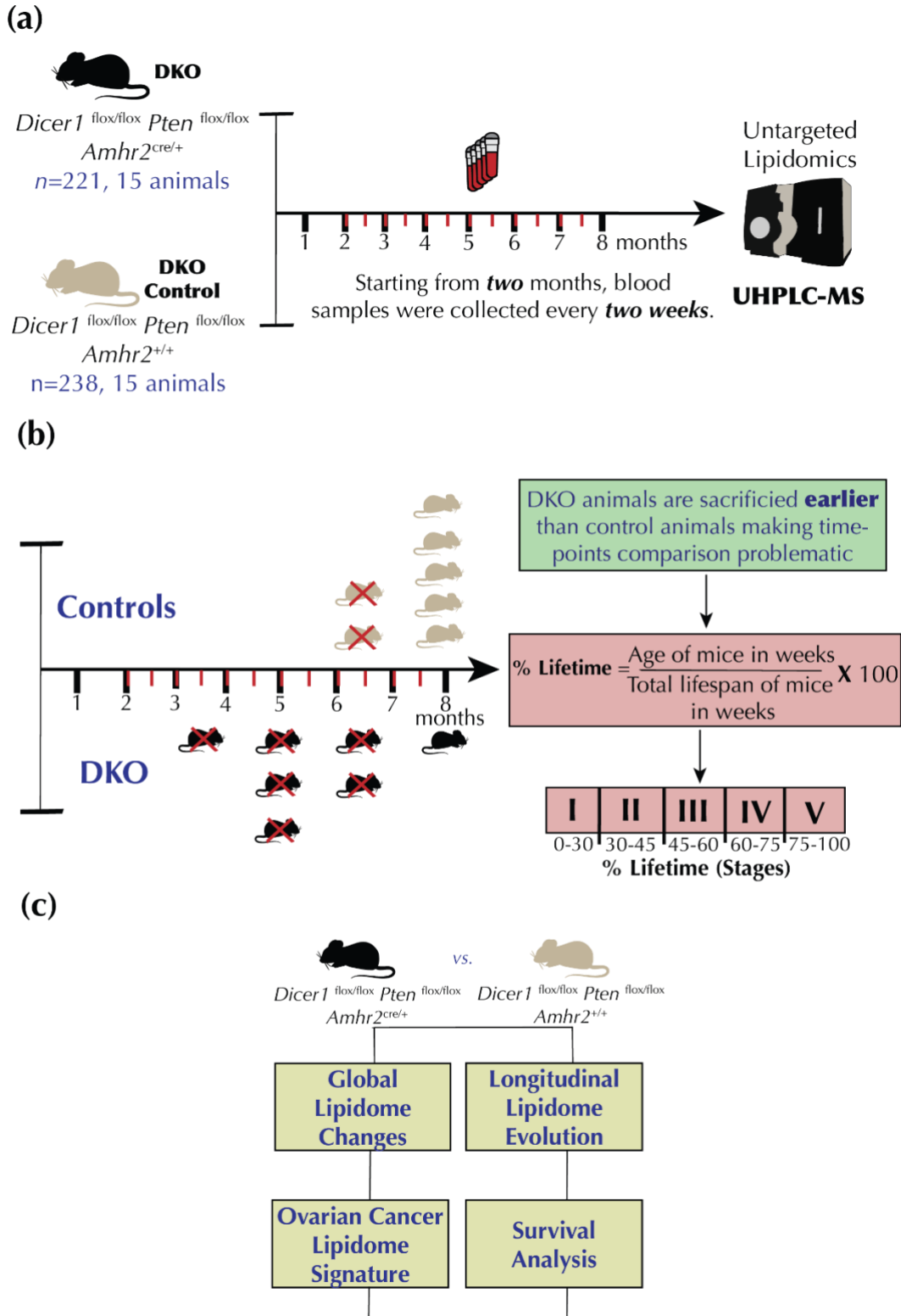
913 Conceptualization: OOB, FMF, DAG
914 Methodology: OOB, FMF, SS, DAG
915 Investigation: SS, OOB, SGM
916 Software: OOB,
917 Visualization: OOB,
918 Supervision: FMF, DAG
919 Writing—original draft: OOB, FMF
920 Writing—review & editing: OOB, FMF, SS, JK, DAG, SGM, MP
921 Funding acquisition: FMF

922
923 **Competing interests:** The authors declare no competing interests.

924 **Data and materials availability:** Data generated in this study are available through the
925 NIH Metabolomics Workbench (<http://www.metabolomicsworkbench.org/>) with project
926 ID PR001457 (study ID ST002276 [<http://dx.doi.org/10.21228/M8D133>]). Code is
927 available on GitHub: <https://github.com/obifarin/DKO-lipidomics>

928
929

Figures and Tables



930

931

932

933

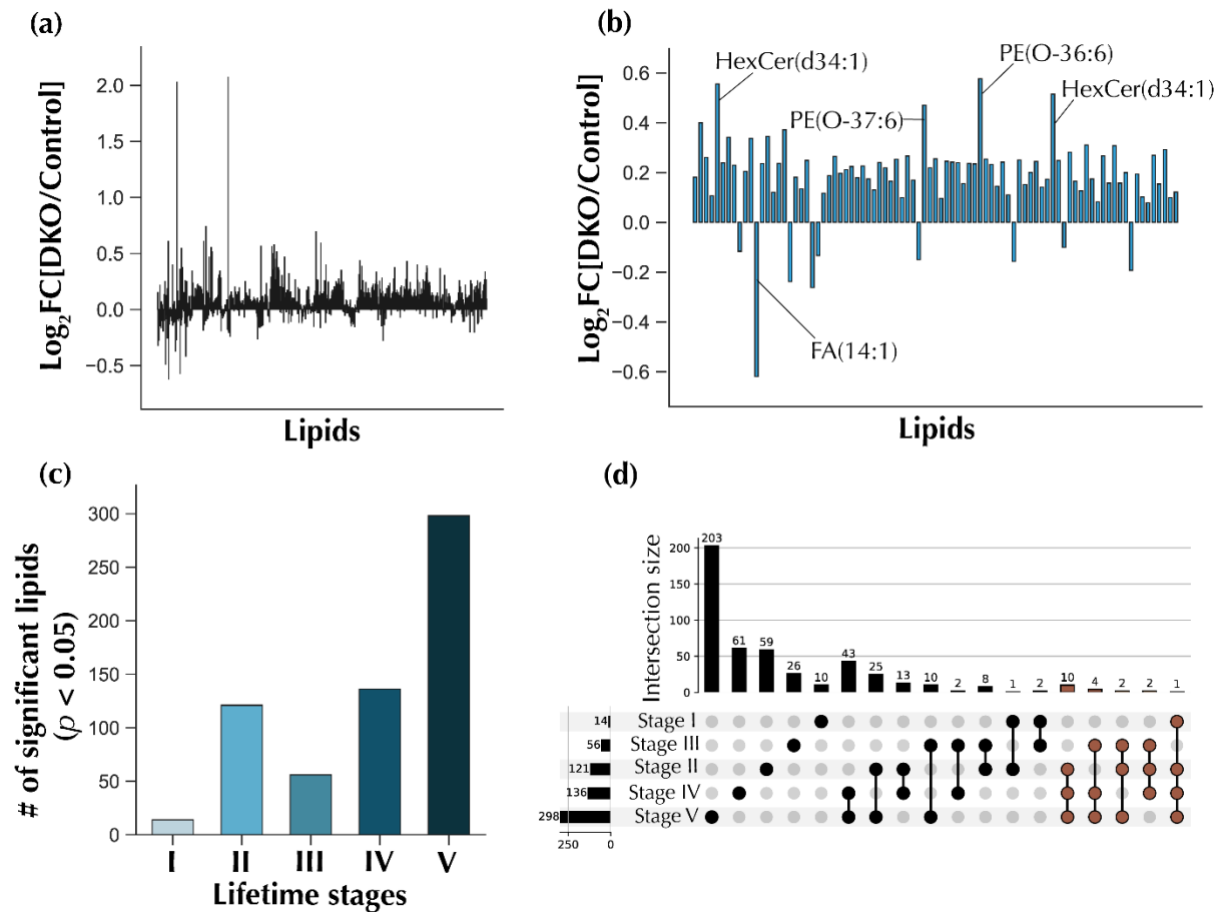
934

935

936

Figure 1. Blood sampling scheme, study design, and analysis plan. (a) Blood samples were collected every two weeks, starting at the two-month mark. Lipidomics experiments were conducted using ultra-high performance liquid chromatography mass spectrometry (UHPLC-MS). (b) Conversion of the mice age in weeks to percentage lifetime makes lipidomic comparisons effective. (c) Computational analysis plan.

937



938

939

940

941

942

943

944

945

946

Fig 2. Global lipidomic changes observed upon HGSC progression. (a) Overall fold changes for all annotated features, for all time points combined. (b) Fold changes for 87 significant lipid features (Welch's *T*-test, Benjamini-Hochberg correction *q*-value < 0.05) for all time points combined. (c) The number of significant lipidomic features (Welch's *T*-test *p*-value < 0.05) for each lifetime stage. (d) Upset plot showing overlapping significant lipids in various lifetime stages. Sets containing lipid features present in at least three lifetime stages are colored brown.

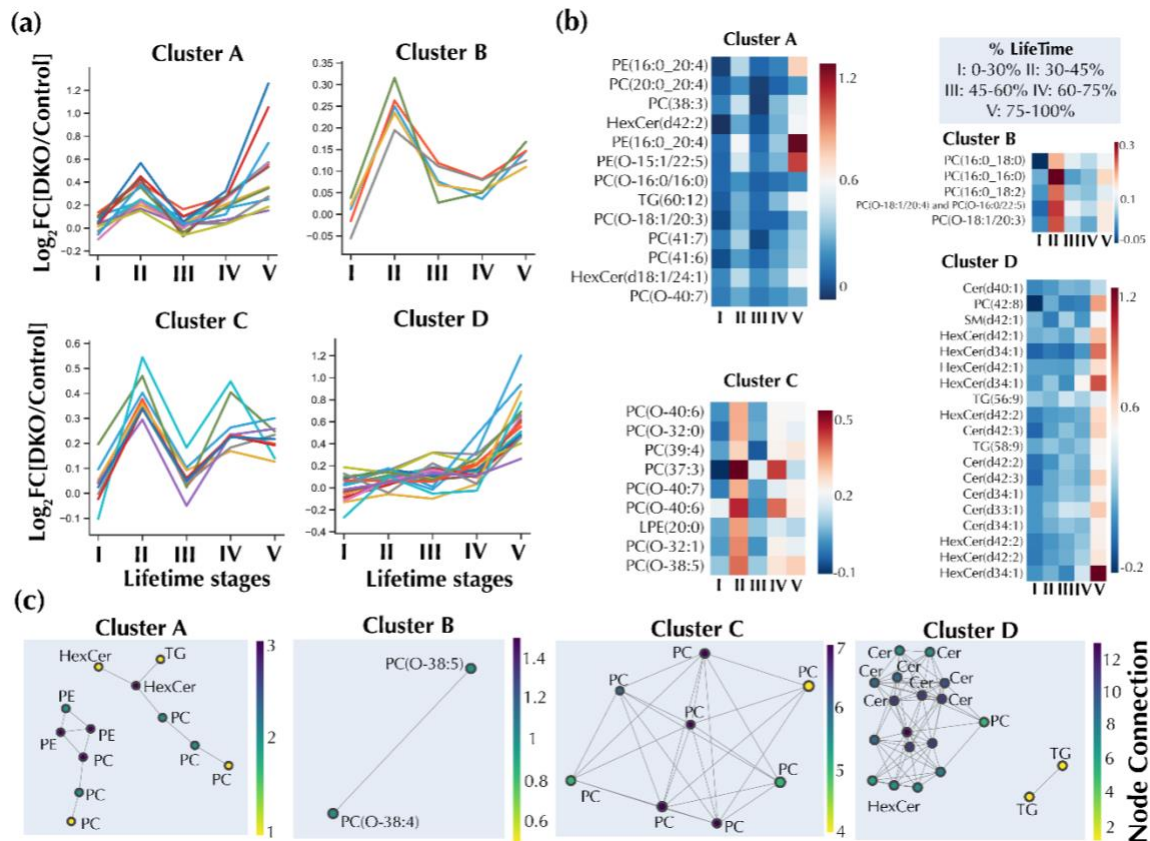


Fig 3. Lipidome changes in response to ovarian cancer progression. (a) Hierarchical clustering analysis shows the grouping of lipidome trajectories into four types of clusters. (b) Longitudinal lipid changes for the selected clusters indicating fold changes. (c) Network graph for the clusters shown in (a). Nodes represent lipids, while the links connect nodes with a high Pearson's correlation ($r \geq 0.5$).

947

948

949

950

951

952

953
954
955
956
957
958
959
960
961
962
963

Table 1. Annotations for lipid clusters associated with ovarian cancer progression.

Proposed lipid annotation, experimental *m/z* value, chromatographic retention time (RT) in minutes (min), and main adduct type detected are shown. DG: Diacylglycerols, TG: Triacylglycerols, FA: Fatty acids, HexCer: Hexosylceramides, LPC: Lysophosphatidylcholines, LPE: Lysophosphatidylethanolamines, PC: Phosphatidylcholines, PC-O: Ether phosphatidylcholines, PE: Phosphatidylethanolamines, PE-O: Ether phosphatidylethanolamines, PI: Phosphatidylinositols, Cer: Ceramides, and SM: Sphingomyelins.

ID	Lipids	Adduct	RT [min]	Mass Error (ppm)	Experimental <i>m/z</i>
Cluster A					
4260	HexCer(d42:2)	[M+CH ₃ COOH-H] ⁻	6.50	3.93	868.6917
2626	PC(20:0_20:4)	[M+H ₂ CO ₂ -H] ⁻	5.20	3.13	882.6257
1876	PC(O-16:0_16:0)	[M+CH ₃ COOH-H] ⁻	5.17	4.31	778.6001
2412	PC(O-18:1/20:3)	[M+CH ₃ COOH-H] ⁻	5.03	3.36	854.6309
2587	PC(O-18:1_22:6) and PC(O-22:7_18:0)	[M+CH ₃ COOH-H] ⁻	4.33	3.31	876.6153
1650	PE(16:0_20:4)	[M-H] ⁻	4.35	4.46	738.5122
1651	PE(16:0_20:4)	[M-H] ⁻	4.17	4.62	738.5113
1623	PE(O-15:1_22:5)	[M-H] ⁻	4.35	4.71	734.5164
10366	TG(60:12)	[M+NH ₄] ⁺	7.56	2.82	968.7729
6813	HexCer(d18:1_24:1)	[M+H] ⁺	6.54	4.42	810.6853
6839	PC(38:3)	[M+H] ⁺	4.95	-1.03	812.6155
7604	PC(41:6)	[M+H] ⁺	5.04	1.81	848.6179
7565	PC(41:7)	[M+H] ⁺	5.26	-2.04	846.5990
Cluster B					
1870	PC(16:0_16:0)	[M+H ₂ CO ₂ -H] ⁻	4.26	3.38	778.5629
2050	PC(16:0_18:0)	[M+H ₂ CO ₂ -H] ⁻	5.45	4.03	806.5949
1679	PC(16:0_18:2)	[M+H ₂ CO ₂ -H] ⁻	4.14	-0.76	802.5597
2411	PC(O-18:1_20:3)	[M+CH ₃ COOH-H] ⁻	4.52	-1.85	854.6264
2400	PC(O-18:1_20:4) and PC(O-16:0_22:5)	[M+CH ₃ COOH-H] ⁻	4.52	3.18	852.6151
Cluster C					
886	LPE(20:0)	[M-H] ⁻	2.27	4.47	508.3431
6573	PC(37:3)	[M+H] ⁺	4.80	2.48	798.6027
7105	PC(39:4)	[M+H] ⁺	5.26	0.83	824.6170
5618	PC(O-32:0)	[M+H] ⁺	5.22	1.41	720.5911
5604	PC(O-32:1)	[M+H] ⁺	4.48	1.61	718.5756

6493	PC(O-38:5)	[M+H] ⁺	4.56	-0.28	794.6060
7022	PC(O-40:6)	[M+H] ⁺	5.26	0.73	820.6220
7023	PC(O-40:6)	[M+H] ⁺	4.62	2.81	820.6237
6984	PC(O-40:7)	[M+H] ⁺	4.40	0.10	818.6059
Cluster D					
1111	Cer(d33:1)	[M+CH ₃ COOH-H] ⁻	4.69	4.80	582.5131
966	Cer(d34:1)	[M-H] ⁻	4.70	2.96,	536.5064,
1149	Cer(d34:1)	[M+CH ₃ COOH-H] ⁻	4.72	4.28	596.5285
1217	Cer(d40:1)	[M-H] ⁻ , [M+CH ₃ COOH-H] ⁻	6.82	4.62, 4.38	620.6014, 680.6229
1297	Cer(d42:2)	[M-H] ⁻	6.79	4.73,	646.6174,
1290	Cer(d42:3)	[M-H] ⁻	6.45	4.27	644.6011
1504	Cer(d42:3)	[M+CH ₃ COOH-H] ⁻	6.46	4.19	704.6228
1473	HexCer(d34:1)	[M-H] ⁻	4.32	3.17	698.5611
1761	HexCer(d34:1)	[M+CH ₃ COOH-H] ⁻	4.09	4.21	758.5819
1762	HexCer(d34:1)	[M+CH ₃ COOH-H] ⁻	4.32	2.37	758.5805
2078	HexCer(d42:1)	[M-H] ⁻	6.83	4.50	810.6857
2532	HexCer(d42:1)	[M+CH ₃ COOH-H] ⁻	6.83	2.53	870.7061
2065	HexCer(d42:2)	[M-H] ⁻	6.40	3.76	808.6698
2522	HexCer(d42:2)	[M+CH ₃ COOH-H] ⁻	6.41	3.83	868.6916
2415	HexCer(d42:2)	[M+H ₂ CO ₂ -H] ⁻	6.40	3.70	854.6758
2557	SM(d42:1)	[M+CH ₃ COOH-H] ⁻	7.16	3.95	873.7100
7815	PC(42:8)	[M+H] ⁺	4.08	1.32	858.6018
9401	TG(56:9)	[M+NH ₄] ⁺	7.59	0.26	918.7547
10226	TG(58:9)	[M+NH ₄] ⁺	7.65	5.36	946.7908

964
965
966
967
968
969

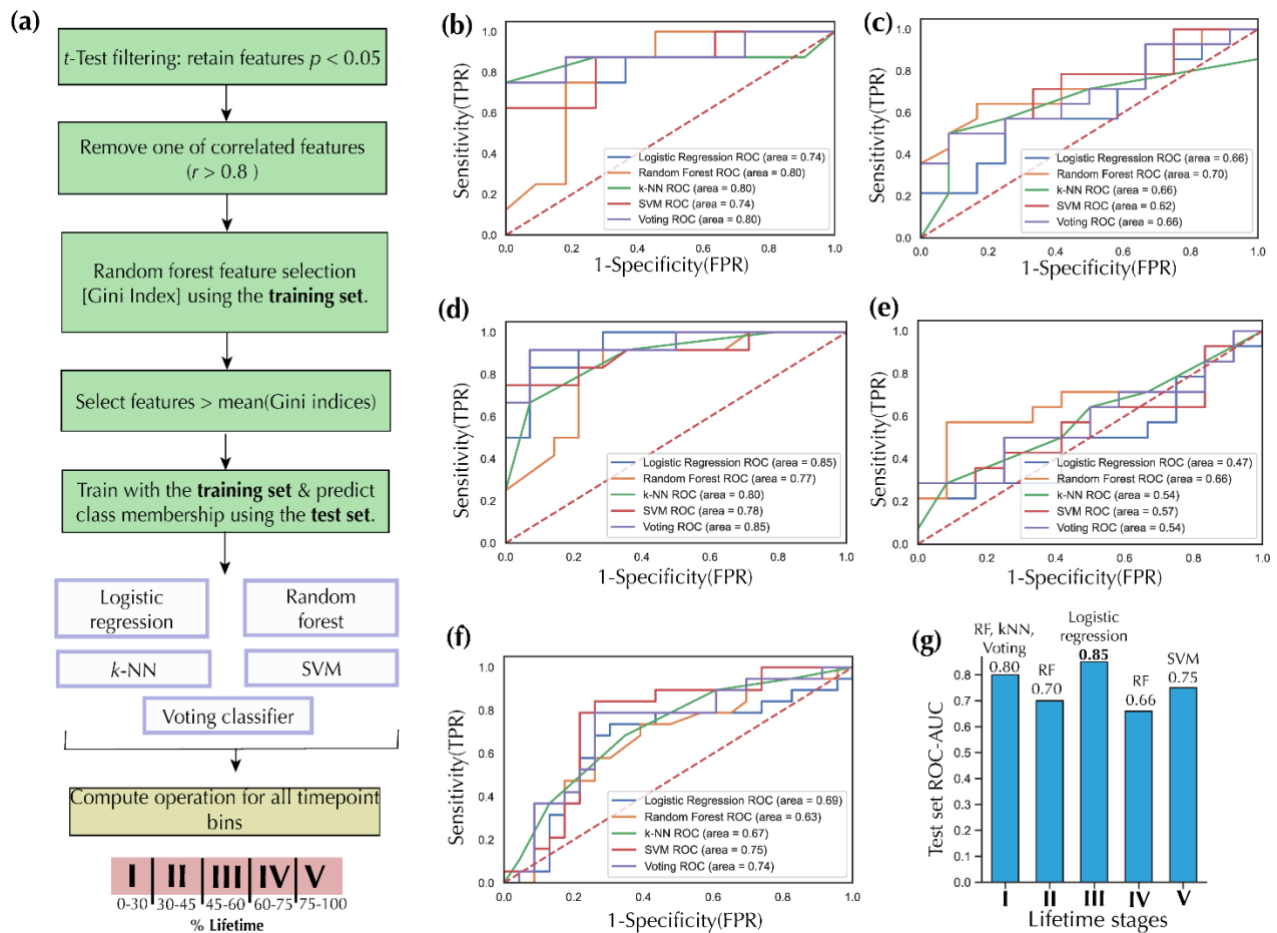


Fig 4. Discriminating DKO from DKO control mice via machine learning. (a) Machine learning pipeline. The pipeline starts with a t -test filtering method for each of the five ML tasks: lipid features with less than 0.05 p -value (Welch's t -test $p < 0.05$) were selected. Next, one of two lipid features with a high Pearson's correlation score ($r > 0.8$) was removed from the dataset to avoid unnecessary redundancies. Finally, lipid features with a Gini index greater or equal to the mean of all Gini indices were selected for training and testing purposes. ROC-AUC test set for DKO classification for (b), lifetime stage I (c), lifetime stage II (d), lifetime stage III (e), lifetime stage IV (f), and lifetime stage V. (g) The best ROC-AUC scores for each lifetime stage. TPR: True positive rate, FPR: False positive rate, k -NN: k -Nearest Neighbors, RF: Random Forests, SVM: Support Vector Machine, Voting: Voting Ensemble Classifier.

970

971

972

973

974

975

976

977

978

979

980

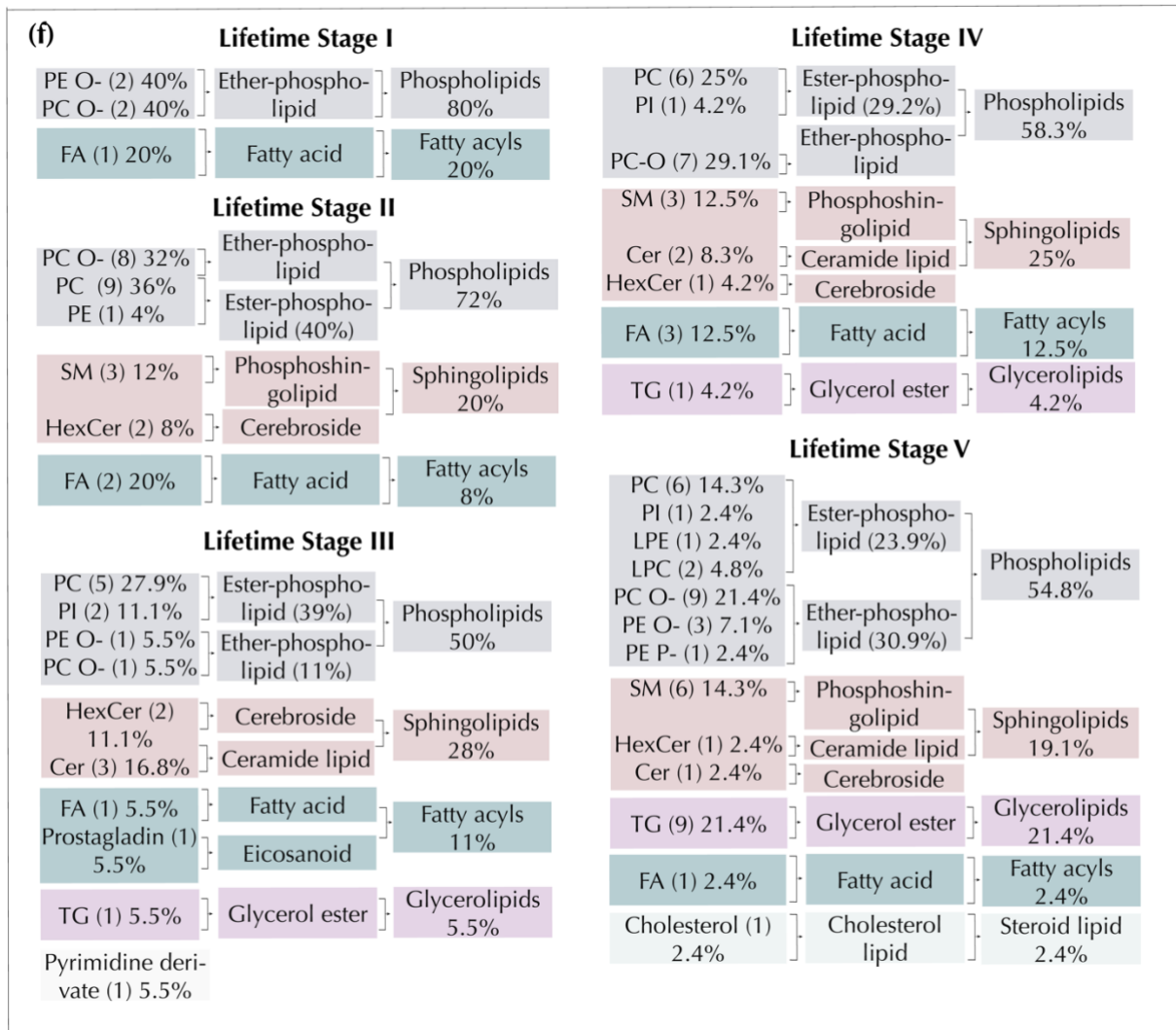
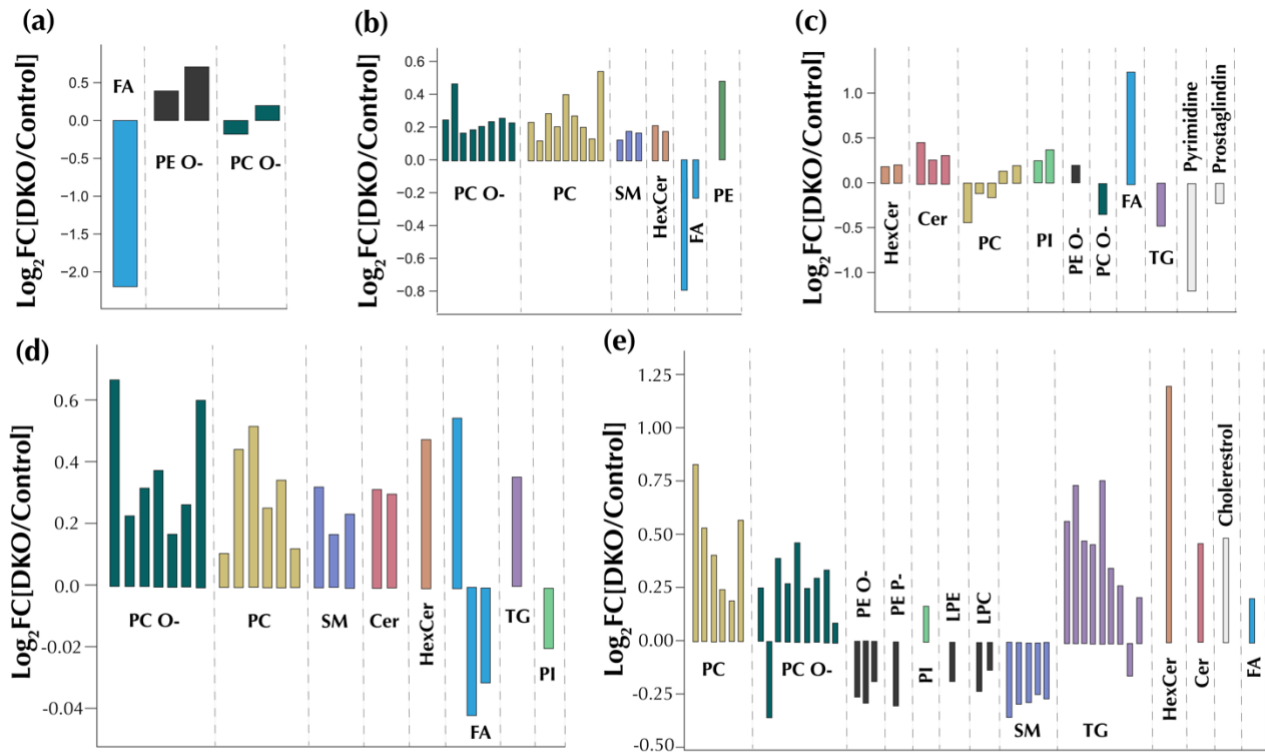
981

982

983

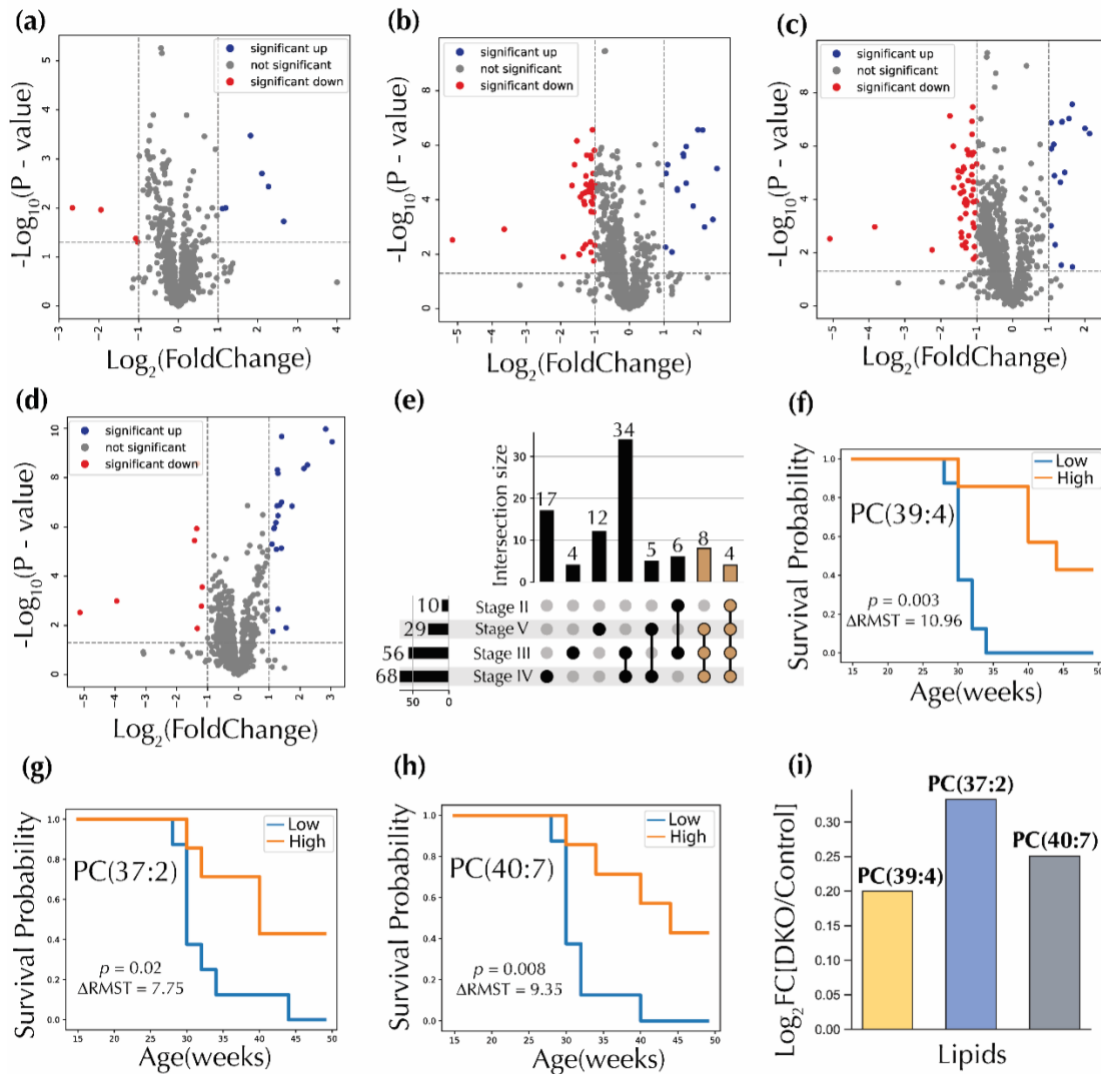
984

985



987 **Fig 5. Discriminant lipids for each of the five lifetime stages. (a)** Lifetime stage I: 0-
988 30% lifetime. **(b)** Lifetime stage II: 30-45% lifetime. **(c)** lifetime stage III: 45-60%
989 lifetime **(d)** Lifetime stage IV: 60-75% lifetime. **(e)** Lifetime stage V: 75-100%
990 lifetime. **(f)** frequency of lipid classes, groups, and categories in the discriminant
991 lipid panels. TG: Triacylglycerols, FA: Fatty acids, HexCer: Hexosylceramides,
992 LPC: Lysophosphatidylcholines, LPE: Lysophosphatidylethanolamines, PC:
993 Phosphatidylcholines, PC-O: Ether phosphatidylcholines, PE:
994 Phosphatidylethanolamines, PE-O: Ether phosphatidylethanolamines, PI:
995 Phosphatidylinositols, Cer: Ceramides, and SM: Sphingomyelins
996

997



998

999

1000

1001

1002

1003

1004

1005

1006

1007

Fig 6. Prognostic circulating lipid candidates. Volcano plots comparing DKO lifetime stage I with (a) DKO lifetime stage II, (b) DKO lifetime stage III, (c) DKO lifetime stage IV and (d) DKO lifetime stage V. *P*- values for volcano plot analysis were calculated using Welch's *T*-test. (e) Upset plot showing the intersection of the various groups of significant lipids selected from volcano plots. Lipids present in at least three sets were colored brown. Kaplan-Meier survival curves for (f) PC(39:4), (g) PC(37:2) and (h) PC(40:7). *P*-values were computed with the Log rank test. (i) Selected prognostic circulating lipids. PC: Phosphatidylcholines FC: Fold changes. ΔRMST : differences in restricted mean survival times.

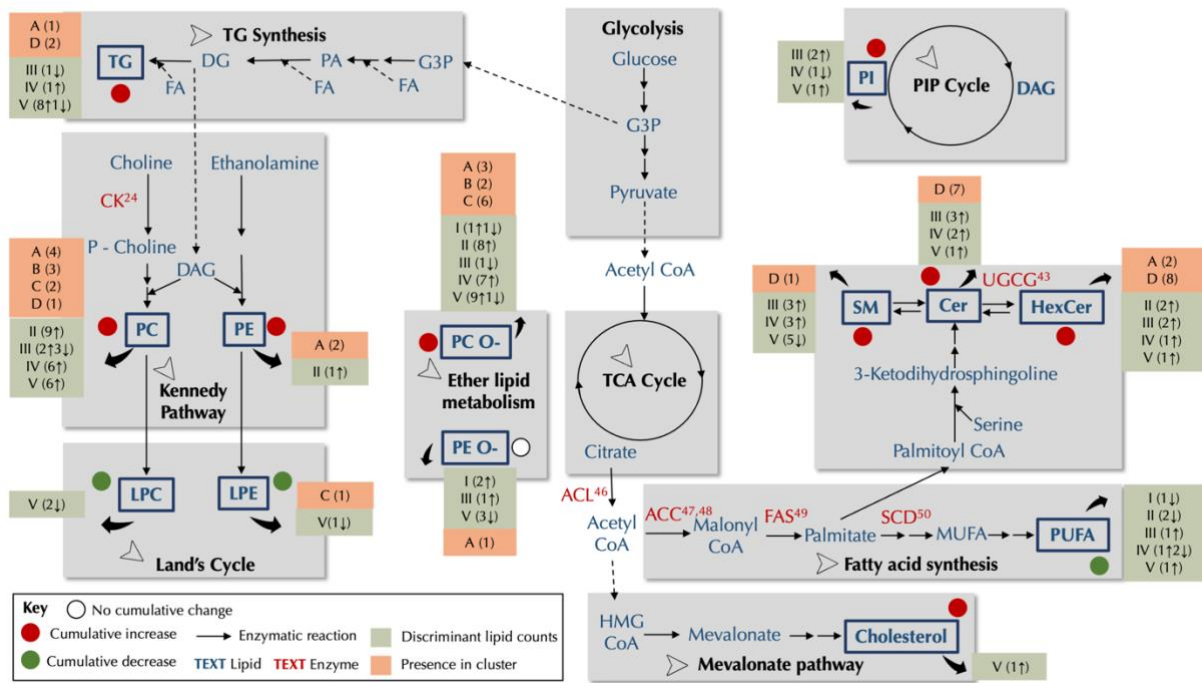


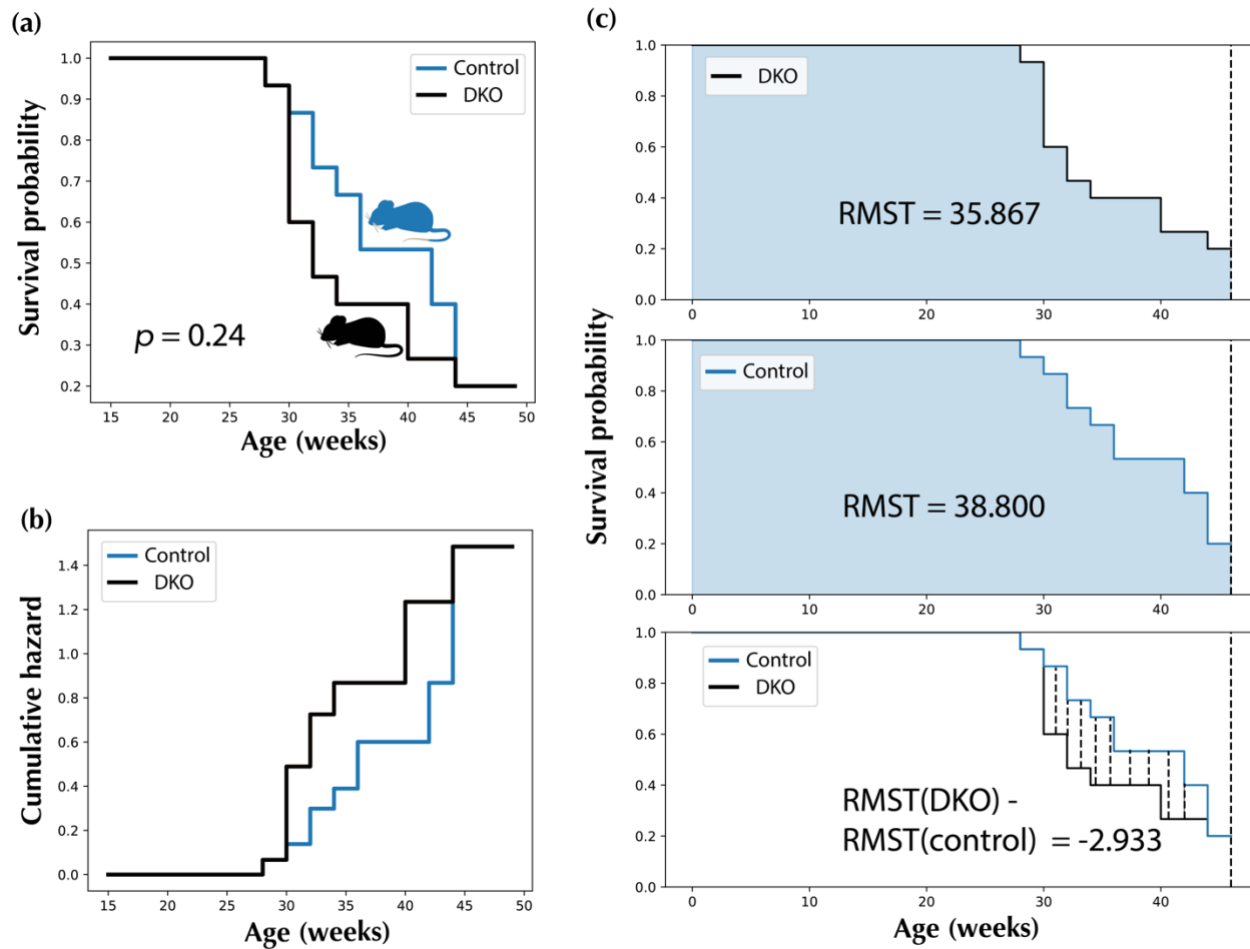
Fig 7. Schematic of metabolic pathways showing key metabolic alterations in the DKO

mice lipidome. Lipid classes detected in the study are indicated as bolded blue text, while unbolded blue text signifies other metabolites in the metabolic pathway. Red text indicates enzymes known to be overly expressed in ovarian cancer cells or other related cancer, with the relevant references. For each detected lipid class presented, information about the cluster they belong to in the temporal trend analyses is provided, in addition to the breakdown information on discriminant lipids selected by ML algorithms. A red circle represents the cumulative change in detected lipid classes (increase in DKO mice), a green circle (decrease in DKO mice), or a white circle (no cumulative change). Cumulative changes are computed by counting the number of both increased and decreased levels among the selected discriminant lipid in all lifetime stages. Pathway information was derived from existing literature. Abbreviations: G3P: Glycerol-3-phosphate, PA: Phosphatidic acid, DG: Diacylglycerols, TG: Triacylglycerols, PC: Phosphatidylcholines, PC O-: Ether phosphatidylcholines, PE: Phosphatidylethanolamines, PE O-: Ether phosphatidylethanolamines, LPE: Lysophosphatidylethanolamines, LPC: Lysophosphatidylcholines, PI: Phosphatidyl inositol, HMG CoA: 3-hydroxy-3-methylglutaryl coenzyme A, MUFA: mono-unsaturated fatty acids, PUFA: Poly-unsaturated fatty acids, SM: Sphingomyelin, Cer: Ceramide, HexCer: Hexosylceramide, CK: Choline kinase, ACC: acetyl-CoA carboxylase, ACL: ATP-citrate lyase, FAS: Fatty acid synthase, SCD1: Stearoyl-CoA desaturase-1, UGCG: uridine diphosphate-glucose ceramide glucosyltransferase.

1008
1009
1010
1011
1012
1013
1014
1015
1016
1017
1018
1019
1020
1021
1022
1023
1024
1025
1026
1027
1028
1029
1030
1031
1032
1033
1034
1035
1036

1037

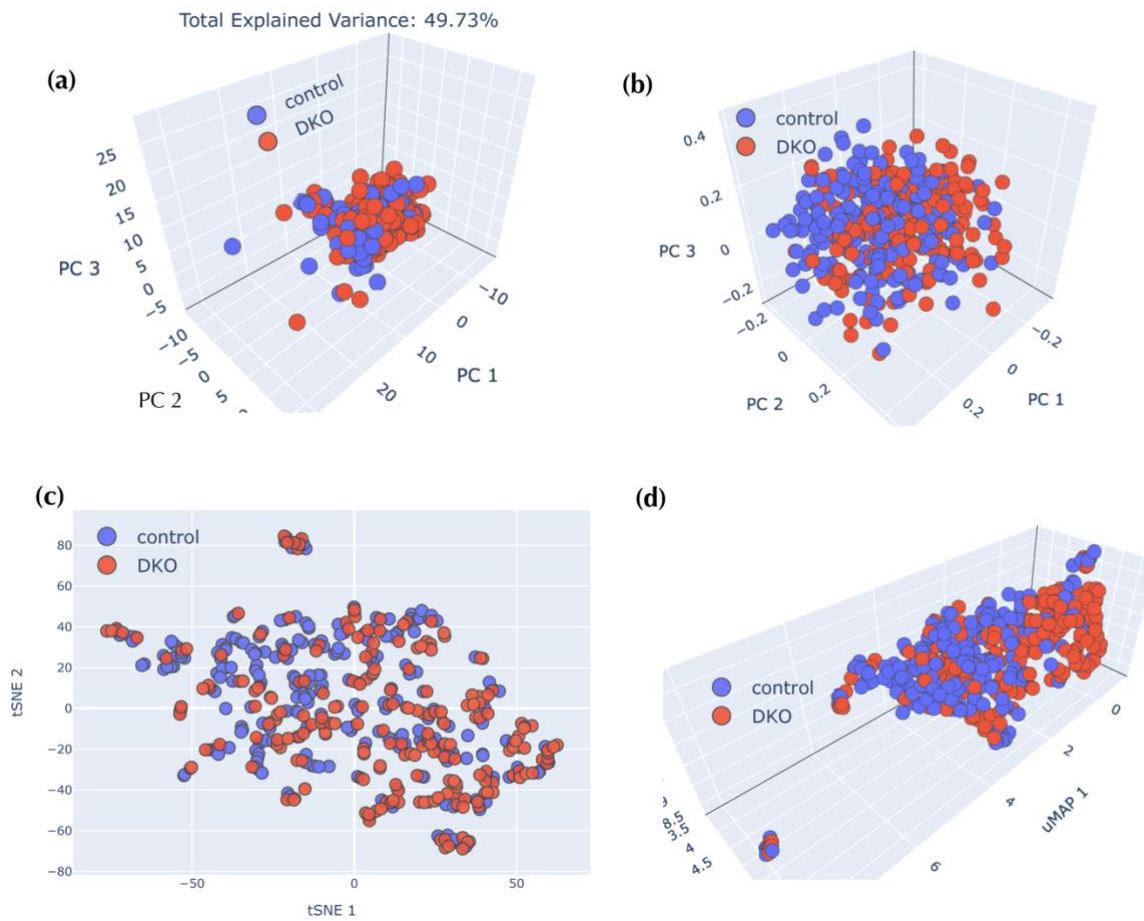
Supplementary Materials



1038

1039 **Figure S1. Survival analysis comparison of DKO and DKO control mice.** (a) Kaplan-Meier
1040 survival curve estimate, DKO vs. DKO control mice. (b), Nelson-Aalen hazard curve estimate,
1041 DKO vs. DKO control mice. (c), Restricted Mean Survival Times (RMST), DKO vs. DKO
1042 control mice.

1043



1044

1045

1046

1047

1048

1049

Figure S2. DKO and DKO control mice comparison via unsupervised learning methods. (a), PCA score plot. (b), Kernel PCA score plot. (c), tSNE score plot. (d), UMAP score plot. Eighty-seven statistically significant lipid abundances were used for unsupervised learning, and all-time points were combined.

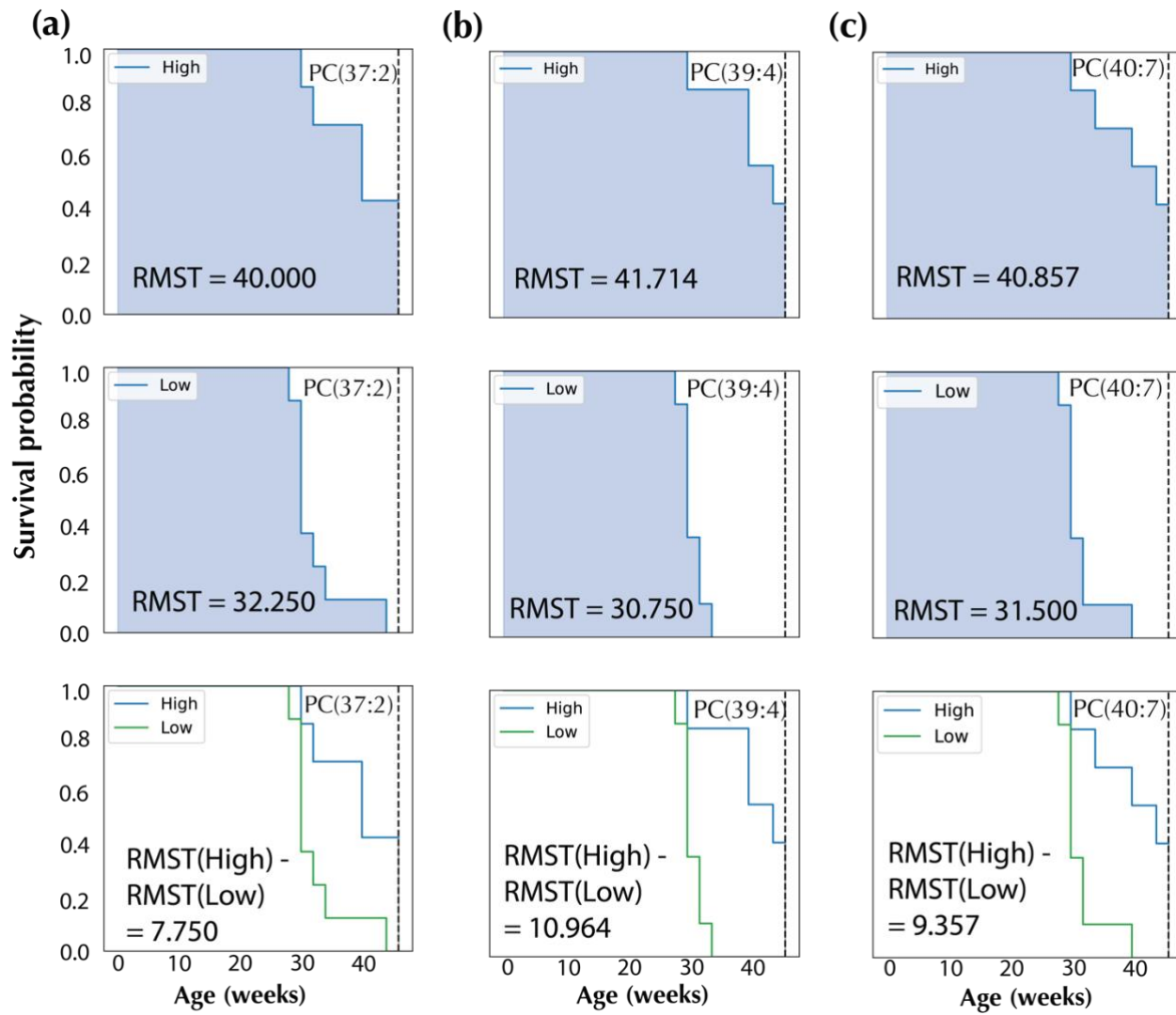


Figure S3. Restricted Mean Survival Times (RMST) plots for all prognostic lipid candidates. (a), PC(37:2). (b), PC(39:4). (c), PC(40:7).

1054 **Table S1. Eighty-seven statistically significant ($q < 0.05$) lipids for the DKO vs. DKO control**
 1055 **comparison, all time points combined.** DG: Diacylglycerols, TG: Triacylglycerols, FA: Fatty
 1056 acids, HexCer: Hexosylceramides, LPC: Lysophosphatidylcholines, LPE:
 1057 Lysophosphatidylethanolamines, PC: Phosphatidylcholines, PC-O: Ether phosphatidylcholines,
 1058 PE: Phosphatidylethanolamines, PE-O: Ether phosphatidylethanolamines, PI:
 1059 Phosphatidylinositols, Cer: Ceramides, and SM: Sphingomyelins.

1060

ID	Retention Time [min]	Lipids	Adduct
24	1.54	FA(14:1)	[M-H] ⁻
1472	4.67	PE(O-34:3)	[M-H] ⁻
1111	4.69	Cer(d33:1)	[M+CH ₃ COOH-H] ⁻
966	4.70	Cer(d34:1)	[M-H] ⁻
1149	4.72	Cer(d34:1)	[M+CH ₃ COOH-H] ⁻
1217	6.83	Cer(d40:1)	[M-H] ⁻
1454	6.64	Cer(d41:2)	[M+CH ₃ COOH-H] ⁻
1297	6.79	Cer(d42:2)	[M-H] ⁻
1290	6.46	Cer(d42:3)	[M-H] ⁻
1504	6.46	Cer(d42:3)	[M+CH ₃ COOH-H] ⁻
111	2.37	FA(18:1)	[M-H] ⁻
1473	4.33	HexCer(d34:1)	[M-H] ⁻
1761	4.09	HexCer(d34:1)	[M+CH ₃ COOH-H] ⁻
1762	4.32	HexCer(d34:1)	[M+CH ₃ COOH-H] ⁻
2078	6.83	HexCer(d42:1)	[M+CH ₃ COOH-H] ⁻
2532	6.83	HexCer(d42:1)	[M-H] ⁻
2065	6.41	HexCer(d42:2)	[M-H] ⁻
2522	6.41	HexCer(d42:2)	[M+CH ₃ COOH-H] ⁻
4260	6.51	HexCer(d42:2)	[M-H] ⁻
2415	6.41	HexCer(d42:2)	[M+H ₂ CO ₂ -H] ⁻
257	2.03	FA(20:4-2OH)	[M-H] ⁻
52	2.02	FA(16:1)	[M-H] ⁻
1870	4.26	PC(16:0_16:0)	[M+H ₂ CO ₂ -H] ⁻
2050	5.45	PC(16:0_18:0)	[M+H ₂ CO ₂ -H] ⁻
2110	3.76	PC(16:0_18:2)	[M+CH ₃ COOH-H] ⁻
1679	4.14	PC(16:0_18:2)	[M+H ₂ CO ₂ -H] ⁻
1751	4.51	PC(16:0_18:2)	[M+H ₂ CO ₂ -H] ⁻
2265	5.90	PC(18:0_18:0)	[M+H ₂ CO ₂ -H] ⁻
2163	3.56	PC(16:0_20:5)	[M+H ₂ CO ₂ -H] ⁻
2225	5.32	PC(17:0_18:2)	[M+CH ₃ COOH-H] ⁻
4126	4.56	PC(18:0_20:4)	[2M+H ₂ CO ₂ -H] ⁻
2725	5.09	PC(18:0_22:4)	[M+CH ₃ COOH-H] ⁻
2626	5.20	PC(20:0_20:4)	[M+H ₂ CO ₂ -H] ⁻
1876	5.18	PC(O-16:0_16:0)	[M+CH ₃ COOH-H] ⁻
1849	2.05	PC(O-17:1_15:1) and PC(O-16:1_18:1)	[M+CH ₃ COOH-H] ⁻

2038	2.37	PC(O-16:0_18:1)	[M+CH ₃ COOH-H] ⁻
2205	4.51	PC(O-18:1_18:2)	[M+CH ₃ COOH-H] ⁻
2187	4.50	PC(O-16:1_20:3)	[M+CH ₃ COOH-H] ⁻
2432	5.33	PC(O-18:0_20:3)	[M+CH ₃ COOH-H] ⁻
2411	4.52	PC(O-18:1_20:3)	[M+CH ₃ COOH-H] ⁻
2412	5.04	PC(O-18:1_20:3)	[M+CH ₃ COOH-H] ⁻
2400	4.52	PC(O-18:1_20:4) and PC(O-16:0_22:5)	[M+CH ₃ COOH-H] ⁻
2587	4.33	PC(O-18:1_22:6) and PC(O-22:7_18:0)	[M+CH ₃ COOH-H] ⁻
1650	4.36	(16:0_20:4)	[M-H] ⁻
1651	4.17	(16:0_20:4)	[M-H] ⁻
1623	4.35	PE(O-15:1_22:5)	[M-H] ⁻
1699	4.33	PE(O-18:3_20:4)	[M-H] ⁻
1641	4.38	PE(O-22:8_18:0) and PE(O-18:2_22:6)	[M-H] ⁻
1837	4.36	PE(O-22:8_18:0) and PE(O-18:2_22:6)	[M-H] ⁻
2631	3.50	PI(18:1_20:4)	[M-H] ⁻
349	2.38	Prostaglandin A1 ethyl ester	[M-H] ⁻
1912	4.00	SM(d36:2)	[M+CH ₃ COOH-H] ⁻
2439	6.14	SM(d41:2)	[M+CH ₃ COOH-H] ⁻
2557	7.17	SM(d42:1)	[M+CH ₃ COOH-H] ⁻
78	2.21	FA(17:1)	[M-H] ⁻
886	2.27	LPE(20:0)	[M-H] ⁻
5443	9.32	DG(40:0)	[M+NH ₄] ⁺
10366	7.56	TG(60:12)	[M+NH ₄] ⁺
5438	9.29	Campesterol Ester(18:2)	[M+NH ₄] ⁺
5439	9.35	Campesterol Ester(18:2)	[M+NH ₄] ⁺
5344	6.87	Cer(d18:1_24:1)	[M+H] ⁺
6813	6.54	HexCer(d18:1_24:1)	[M+H] ⁺
6573	4.80	PC(37:3)	[M+H] ⁺
6839	4.95	PC(38:3)	[M+H] ⁺
7105	5.26	PC(39:4)	[M+H] ⁺
7357	4.52	PC(40:5)	[M+H] ⁺
7604	5.05	PC(41:6)	[M+H] ⁺
7565	5.26	PC(41:7)	[M+H] ⁺
7815	4.08	PC(42:8)	[M+H] ⁺
5618	5.22	PC(O-32:0)	[M+H] ⁺
5604	4.49	PC(O-32:1)	[M+H] ⁺
6538	5.08	PC(O-38:4)	[M+H] ⁺
6539	5.09	PC(O-38:4)	[M+H] ⁺
6493	4.57	PC(O-38:5)	[M+H] ⁺
7022	5.26	PC(O-40:6)	[M+H] ⁺
7023	4.63	PC(O-40:6)	[M+H] ⁺
6983	4.06	PC(O-40:7)	[M+H] ⁺

6984	4.40	PC(O-40:7)	[M+H] ⁺
9401	7.59	TG(56:9)	[M+NH ₄] ⁺
8964	7.46	TG(58:11)	[2M+K] ⁺
9614	7.46	TG(58:11)	[2M+NH ₄] ⁺
10101	7.46	TG(58:11)	[M+K] ⁺
10226	7.65	TG(58:9)	[M+NH ₄] ⁺
10227	7.69	TG(58:9)	[M+NH ₄] ⁺
10228	7.79	TG(58:9)	[M+NH ₄] ⁺
10230	7.99	TG(58:9)	[M+NH ₄] ⁺
4512	9.48	cholesterol derivative	[M+NH ₄] ⁺

1061

1062

1063

1064 **Table S2. Statistically significant lipid features for the comparison between DKO and DKO**
1065 **control mice that were present in at least three lifetime stages.** FA: Fatty acids, PC:
1066 Phosphatidylcholines, PC-O: Ether phosphatidylcholines, Cer: Ceramides, and SM:
1067 Sphingomyelins.

1068

ID	Retention Time [min]	Lipids
201	1.13	15-deoxy-D-12,14-Prostaglandin A2
1111	4.69	Cer(d33:1)
1454	6.64	Cer(d41:2)
2163	3.56	PC(16:0_20:5)
2409	4.77	PC(18:0_20:4)
2725	5.09	PC(18:0/22:4)
1849	2.05	PC(O-17:1_15:1) and PC(O-16:1_18:1)
2587	4.33	PC(O-18:1_22:6) and PC(O-22:7_18:0)
349	2.38	Prostaglandin A1 ethyl ester
2238	6.32	SM(t39:0) or SM(d39:0-OH)
4431	1.64	FA(18:3)
5618	5.22	PC(O-32:0)
5604	4.49	PC(O-32:1)
6538	5.08	PC(O-38:4)
6539	5.09	PC(O-38:4)
6493	4.57	PC(O-38:5)
7022	5.26	PC(O-40:6)
7023	4.63	PC(O-40:6)
6983	4.06	PC(O-40:7)

1069

1070

1071
1072

Table S3. Lipids selected *via* machine learning for each percentage lifetime stage.

ID	Retention Time [min]	Lipids
Lifetime Stage I: 0-30% Lifetime		
12	1.04	3-hydroxyphenyl-valerate
1472	4.67	PE(O-34:3)
2226	4.51	PC(17:0_18:2)
1941	3.88	PC(38:6)
1560	4.16	PE(O-16:1_20:5)
Lifetime Stage II: 30-45% Lifetime		
452	4.36	FA(26:1)
2463	6.75	HexCer(d40:0-OH)
2446	6.37	HexCer(d40:1-OH)
1679	4.14	PC(16:0_18:2)
2091	3.76	PC(16:0_18:3)
2294	3.42	PC(18:2_18:2)
1789	3.66	PC(16:0_20:5)
2165	3.41	PC(16:1_20:4)
4125	4.78	PC(18:0_20:4)
2143	4.09	PC(18:1_20:4) and PC(16:0_22:5)
2725	5.09	PC(18:0_22:4)
1876	5.18	PC(O-16:0_16:0)
2207	4.65	PC(O-18:1_18:2)
2187	4.50	PC(O-16:1_20:3)
2411	4.52	PC(O-18:1_20:3)
2412	5.04	PC(O-18:1_20:3)
2384	3.98	PC(O-16:1_22:5)
2587	4.33	PC(O-18:1_22:6) and PC(O-22:7_18:0)
1859	4.35	PE(17:0_22:6)
1765	3.42	SM(d34:2)
2540	6.23	SM(d42:2)
2541	6.50	SM(d42:2)
4431	1.64	FA(18:3)
6573	4.80	PC(37:3)
7022	5.26	PC(O-40:6)
Lifetime Stage III: 45-60% Lifetime		
1111	4.70	Cer(d33:1)
1454	6.64	Cer(d41:2)
1726	4.82	Cer(d45:1)
2246	6.12	HexCer(d38:0-OH)
2773	7.14	HexCer(d40:0) or HexCer(t42:0-OH)
2265	5.90	PC(18:0_18:0)
2443	4.04	PC(16:0_20:4)

2409	4.77	PC(18:0_20:4)
2725	5.09	PC(18:0_22:4)
1608	5.64	PE(O-18:0_18:2)
2629	3.56	PI(18:1_20:4)
2631	3.50	PI(18:1_20:4)
349	2.38	Prostaglandin A1 ethyl ester
4450	2.54	6-methyl-1-(2-methylphenyl)-3-propylfuro[3,2-d]pyrimidine-2,4(1H,3H)-dione
4434	1.89	FA(18:2)
6433	4.11	PC(37:6)
6445	4.44	PC(O-38:6)
8429	8.52	TG(18:0_18:1_18:2)_and_TG(18:1_18:1_18:1)_and_TG(16:0_18:2_20:1)
Lifetime Stage IV: 60-75% Lifetime		
277	1.32	FA(20:1-2OH)
229	1.66	FA(20:1-OH)
270	1.69	FA(20:2-2OH)
1111	4.69	Cer(d33:1)
1726	4.82	Cer(d45:1)
1762	4.32	HexCer(d34:1)
2725	5.09	PC(18:0_22:4)
2704	4.81	PC(18:0_22:5)
1727	4.36	PC(O-15:1_20:4)
2587	4.33	PC(O-18:1_22:6) and PC(O-22:7_18:0)
2630	3.35	PI(18:1_20:4)
2439	6.14	SM(d41:2)
2238	6.32	SM(t39:0) or SM(d39:0-OH)
6241	4.40	PC(O-37:5)
6573	4.80	PC(37:3)
6156	5.62	PC(37:4)
6435	4.10	PC(37:6)
7103	4.73	PC(39:4)
5618	5.22	PC(O-32:0)
6538	5.08	PC(O-38:4)
6539	5.09	PC(O-38:4)
6983	4.06	PC(O-40:7)
5593	4.32	SM(d35:1)
8964	7.46	TG(58:11)
Lifetime Stage V: 75-100% Lifetime		
772	1.65	LPE(18:1)
1874	5.52	PE(P-40:4)
1297	6.79	Cer(d42:2)
1473	4.33	HexCer(d34:1)
934	1.74	LPC(20:4_0:0)_and_LPC(0:0_20:4)
1122	1.50	LPC(20:5_0:0)_and_LPC(0:0_20:5)

357	3.63	FA(24:1)
1790	3.95	PC(14:0_16:0)
2412	5.04	PC(O-18:1_20:3)
2384	3.98	PC(O-16:1_22:5)
2619	6.05	PC(O-18:1_22:4)
2587	4.33	PC(O-18:1_22:6) and PC(O-22:7_18:0)
2706	4.48	PC(O-18:1_22:6) and PC(O-22:7_18:0)
2707	4.33	PC(O-18:1_22:6) and PC(O-22:7_18:0)
1884	6.07	PE(O-18:0_22:4); PE(O-40:4)
2063	6.68	PE(O-18:2_24:2)
2021	5.98	PE(O-20:1_22:6)
2436	3.31	PI(16:0_20:4)
1912	4.00	SM(d36:2)
2029	5.03	SM(d37:1)
2116	5.45	SM(d38:1)
2454	6.62	SM(d41:1)
9666	8.02	TG(58:10)
9784	8.24	TG(58:8)
10458	8.55	TG(60:10)
10366	7.56	TG(60:12)
6612	4.57	PC(37:2)
6839	4.95	PC(38:3)
7402	5.72	PC(40:4)
7357	4.52	PC(40:5)
7915	4.65	PC(42:6)
6539	5.09	PC(O-38:4)
6493	4.57	PC(O-38:5)
6983	4.06	PC(O-40:7)
5652	4.08	SM(d36:2)
5891	4.69	SM(d38:4)
7197	8.37	TG(16:0_16:0_18:1)
10287	8.18	TG(18:0_20:4_20:4) and TG(18:0_18:2_22:6)
10226	7.65	TG(58:9)
10227	7.69	TG(58:9)
10230	7.99	TG(58:9)
4512	9.48	cholesterol derivative

1073
1074
1075

1076 **Table S4.**

1077 **Machine learning results for DKO classification.** k-NN: k-Nearest Neighbors, RF: Random
 1078 Forests, SVM: Support Vector Machine, Voting: Voting Classifier. CV: cross-validation. All
 1079 scores are ROC AUC.

1080

Machine learning algorithm	Training set CV scores	Test set scores
Lifetime Stage I: 0-30% Lifetime		
Logistic regression	0.78(\pm 0.16)	0.74
RF	0.82(\pm 0.17)	0.80
k-NN	0.77(\pm 0.24)	0.80
SVM	0.73(\pm 0.19)	0.74
Voting	0.76(\pm 0.20)	0.80
Lifetime Stage II: 30-45% Lifetime		
Logistic regression	0.76(\pm 0.21)	0.66
RF	0.87(\pm 0.09)	0.70
k-NN	0.79(\pm 0.12)	0.66
SVM	0.80(\pm 0.11)	0.62
Voting	0.82(\pm 0.13)	0.66
Lifetime Stage III: 45-60% Lifetime		
Logistic regression	0.66(\pm 0.08)	0.85
RF	0.76(\pm 0.13)	0.77
k-NN	0.81(\pm 0.09)	0.80
SVM	0.80(\pm 0.06)	0.78
Voting	0.77(\pm 0.09)	0.82
Lifetime Stage IV: 60-75% Lifetime		
Logistic regression	0.80(\pm 0.08)	0.47
RF	0.83(\pm 0.13)	0.66
k-NN	0.76(\pm 0.14)	0.54
SVM	0.78(\pm 0.07)	0.57
Voting	0.82(\pm 0.11)	0.54
Lifetime Stage V: 75-100% Lifetime		
Logistic regression	0.90(\pm 0.06)	0.69
RF	0.90(\pm 0.04)	0.63
k-NN	0.90(\pm 0.06)	0.67
SVM	0.90(\pm 0.05)	0.75
Voting	0.91(\pm 0.04)	0.74

1081

1082

1083

1084

1085

1086 **Table S5.**

1087 Composition of stable isotope-labeled chemical standards mixture used in UHPLC-MS.

1088

Isotopically labeled lipids	CAS number	Concentration in stock solution (mg/ml)
LPC (18:1(d7))	2097561-13-0	25
LPE(18:1(d7))	2260669-47-2	5
PC (15:0/18:1(d7))	2097561-16-3	160
PE (15:0/18:1(d7))	2097561-15-2	5
PS (15:0/18:1(d7))	2260669-40-5	10
PG (15:0/18:1(d7))	2260669-42-7	30
PI (15:0/18:1(d7))	2260669-44-9	20
CE (18:1(d7))	1416275-35-8	350
DG (15:0/18:1(d7))	2097561-14-1	10
TG (15:0/18:1(d7)/15:0)	2097561-17-4	55
SM (18:1(d9))	2260669-50-7	30
cholesterol-d7	83199-47-7	100

1089

1090

1091 **Table S6.**

1092 **Chromatographic gradient for RP UHPLC-MS method.** For negative ion mode, mobile phase
1093 A was 10 mM ammonium acetate with water/acetonitrile (40:60 v/v) and mobile phase B was 10
1094 mM ammonium acetate with 2-isopropanol/acetonitrile (90:10 v/v). For positive ion mode,
1095 mobile phase A was 10 mM ammonium formate with water/acetonitrile (40:60 v/v) and 0.1%
1096 formic acid. Mobile phase B was 10 mM ammonium formate with 2-isopropanol/acetonitrile
1097 (90:10 v/v) and 0.1% formic acid.

RP UHPLC Gradient			
Time (min)	Mobile phase A	Mobile phase B	Flow rate (ml min⁻¹)
0.0	80%	20%	0.4
0.0	80%	20%	0.4
1.0	40%	60%	0.4
5.0	30%	70%	0.4
5.5	15%	85%	0.4
8.0	10%	90%	0.4
8.2	0%	100%	0.4
10.5	0%	100%	0.4
10.7	80%	20%	0.4
12.0	80%	20%	0.4

1098

1099 **Table S7.**

1100 **MS parameters used for RP UHPLC-MS.** Arb: Arbitrary units.

1101

MS parameters for RP UHPLC-MS		
MS parameter	Positive mode	Negative mode
Capillary temperature	275 °C	275 °C
Spray voltage	+ 3.5kV	- 2.5kV
Sheath gas flow rate	40 Arb.	40 Arb.
Auxiliary gas flow rate	8 Arb.	8 Arb.
Sweep gas flow rates	1 Arb.	1 Arb.
Vaporizer temperature	320 °C	320 °C

1102

1103